Prior with Far-Field Stress Approximation for Ensemble-Based Data Assimilation in Naturally Fractured Reservoirs

Michael Liem[1], Giulia Conti[1], Stephan Matthai[2], Patrick Jenny[1]

[1]Institute of Fluid Dynamics, ETH Zürich, Zürich, Switzerland
[2]Department of Infrastructure Engineering, University of Melbourne, Melbourne, Victoria, Australia

Key Points:

- Geomechanical proxy model based on projecting tectonic far-field stresses on fracture planes and linear elastic shear displacement
- History matching of apertures in a realistic fracture geometry with over 4000 individual fractures using data from tracer test simulations
- Prior ensembles of aperture realisations from a geomechanical proxy model outperform the ones from naïve stochastic approaches

---

Corresponding author: Michael Liem, `liemm@ethz.ch`

Abstract

Fractures are frequently encountered in reservoirs used for geothermal heat extraction, CO2 storage, and other subsurface applications. Their significant impact on flow and transport requires accurate characterisation for performance estimation and risk assessment. However, fractures, and particularly their apertures, are usually associated with large uncertainties. Data assimilation (or history matching) is a well-established tool for reducing uncertainty and improving simulation results. In recent years, ensemble-based methods like the ensemble smoother with multiple data assimilation (ESMDA) have gained popularity. A key aspect of those methods is a well-constructed prior ensemble that accurately reflects available knowledge. Here, we consider a geological scenario where fracture opening is primarily created by shearing and assume a known fracture geometry. Generating prior realisations of aperture with geomechanical simulators might become computationally prohibitive, while purely stochastic approaches might not incorporate all available geological knowledge. We therefore introduce the far-field stress approximation (FFSA), a proxy model in which this stress is projected onto the fracture planes and shear displacement is approximated with linear elastic theory. We thereby compensate for modelling errors by introducing additional uncertainty in the underlying model parameters. The FFSA efficiently generates reasonable prior realisations at low computational costs. The resulting posterior ensemble obtained from our ESMDA framework matches the flow and transport behaviour of the synthetic reference at measurement locations and improves the estimation of the fracture apertures. These results markedly outperform those obtained from prior ensembles based on two naïve stochastic approaches, thus underlining the importance of accurate prior modelling.

Plain Language Summary

Fractures are often present in subsurface reservoirs, but detecting and characterising them can be challenging. Understanding their location, size, and aperture (i.e., their opening) is crucial for predicting heat production in geothermal reservoirs or preventing leaks during CO2 storage. This study focuses on the fracture apertures as an unknown quantity. We use ensemble-based data assimilation, which involves running numerous simulations with varying parameter values, to get a more complete and accurate understanding of the system, particularly of the fracture apertures. We simulate tracer tests (i.e., injecting fluid with a tracer into the reservoir) using different aperture values and investigate how the initial guess for the aperture values impacts the results. Generating those initial aperture values with geomechanical simulations is accurate but can be computationally expensive. As a fast and reasonably accurate alternative, we use the far-field stress approximation (FFSA), which approximates the costly aspects of the geomechanical simulation. Initial guesses of the aperture values from FFSA outperform the ones from naïve stochastic approaches in our framework, leading to better aperture estimation at lower computational costs. This helps us to accurately model and predict the behaviour of fractures in subsurface reservoirs, contributing to more effective and reliable energy and environmental solutions.

1 Introduction

Proper reservoir characterisation is crucial to accurately model flow and transport, evaluate performance and assess risks in subsurface applications. These applications include geothermal energy extraction (Pruess, 2002; Kumagai et al., 2004; Häring et al., 2008; Amann et al., 2018), geological carbon sequestration (Lu et al., 2013; Bui et al., 2018; Shao et al., 2021), groundwater flow (Flury et al., 1994; Bear & Cheng, 2010), oil and gas reservoirs (Parker, 1989; Ahr, 2008), and nuclear waste disposal (Tsang et al., 2015). Many of these reservoirs contain pre-existing natural fractures or fractures created during construction and operation, which can significantly impact flow and trans-

port (Matthäi & Belayneh, 2004; Geiger et al., 2004; Johnston et al., 2005; Geiger et al., 2010). The extent of their influence depends on fracture parameters such as length, orientation, apertures, location, connectivity, and density. As an example, highly conductive and interconnected fractures can serve as shortcuts for the flow, causing early breakthrough, while small and isolated fractures may have little effect on flow and transport. Precisely estimating these fracture parameters is thus essential.

However, direct measurement of fracture parameters is usually difficult. Several established techniques exist that detect and characterise fractures in the vicinity of boreholes, such as image logging, core analysis or spinner logs (Genter et al., 1997; Prensky, 1999; Al-Dhafeeri & Nasr-El-Din, 2007; Ali et al., 2021). However, boreholes are typically sparse and the space between them is not covered by those methods. Measuring seismic anisotropy on the other hand provides statistical or average information about fractures in the whole reservoir, but only the fracture orientation, density, and, to some extent, length distribution can be deduced, while the apertures and exact geometry of fractures remain unknown (E. Liu & Martinez, 2012). Outcrops show concrete realisations of the fracture geometry, albeit only at the earth's surface. They serve as analogues from which statistical information about the fracture geometry in the subsurface reservoir can be inferred (Casini et al., 2016; Gutmanis et al., 2018). Geostatistical tools such as variograms and (co)kriging analyse and predict distributions of spatially correlated subsurface properties (Chilès & Delfiner, 2012). As a consequence, the fracture parameters, in particular the fracture apertures, are often subject to a high level of uncertainty.

It is therefore necessary to reduce the uncertainty in the fracture parameters for accurate flow and transport modelling in fractured reservoirs. Data assimilation (DA) or history matching is a common tool for reducing uncertainties in model parameters and subsequently improving simulation results by incorporating measurement data. In subsurface applications, often flow and transport measurements from well tests or dynamic production data are used. Popular DA methods include variational data assimilation based on the adjoint method, ensemble-based methods such as the ensemble Kalman filter (EnKF) or particle filter, and hybrid forms thereof (for a review see e.g. Asch et al., 2016; Bannister, 2017; Carrassi et al., 2018; Evensen et al., 2022). The EnKF, introduced by Evensen (1994), is an ensemble approximation of the original Kalman filter (Kalman, 1960) and does not require linearised or adjoint versions of the model or the observation operator. There exists a wide variety of EnKF versions, for a review see e.g. Houtekamer and Zhang (2016), Keller et al. (2018), or Evensen et al. (2022). While the classical EnKF updates the model parameter whenever new measurements are available, ensemble smoothers (ES) collect all measurements in space and time and perform updates only at the end of simulations (van Leeuwen & Evensen, 1996; Skjervheim et al., 2011). This simplifies the implementation as the reservoir simulator does not need to be interrupted. Iterative versions of the ES, such as the ensemble randomised maximum likelihood method (EnRML) (Chen & Oliver, 2012, 2013) or the ensemble smoother with multiple data assimilation (ESMDA) (A. A. Emerick & Reynolds, 2013), were developed for weakly to modestly non-linear systems and have gained popularity in recent years.

Several studies have applied DA to fracture apertures. Some studies assume an identical and known aperture value for all fractures and focus on reducing the uncertainty in other fracture parameters (Ping et al., 2017; Chai et al., 2018; Yao et al., 2018). However, it is known that fracture apertures vary considerably throughout the domain (C. A. Barton et al., 1995; Baghbanan & Jing, 2008; N. Barton & Quadros, 2015; X. Zhang et al., 2021). Other studies have used relatively simple, unconditional distributions to model the apertures (Zhe et al., 2016; Liem & Jenny, 2020; Q. Liu et al., 2022) or set them proportional to the fracture length (K. Zhang et al., 2021). However, these models may not accurately represent the complex relationship between aperture values and stress state, displacement history and fracture parameters such as orientation, length, and surface roughness. In Seabra et al. (2023), those complex relations are included, albeit without

shear displacement. They calculate fracture apertures as a function of effective normal stress obtained from a geomechanical simulation and subsequently reduce the uncertainty in the global model parameters with DA. In Wu et al. (2021), the authors follow an altogether different approach and model aperture variations within the fracture plane of a single fracture.

The performance of ensemble-based DA strongly depends on the quality of the prior ensemble. In the above-mentioned studies, typically either the number of fractures is small or when a moderate number of fractures is used, the apertures only depend on a few underlying uncertain parameters. Ensemble-based DA usually performs well under such conditions; however, it becomes more challenging when considering a large number of fractures each with an individual aperture. The ensemble size is usually limited by computational resources and therefore the prior distribution is likely undersampled. This restricts the solution space as the posterior ensemble is a linear combination of the prior ensemble (Evensen, 2003) and can lead to spurious correlations. Those issues are by no means unique to DA in fractured reservoirs, but they arise in any other application where a huge number of parameters is represented by a limited ensemble size, such as in meteorology, oceanography, or groundwater flows. A common strategy is to apply localisation and inflation methods in the update step (e.g. Anderson & Anderson, 1999; Houtekamer & Mitchell, 2001; Chen & Oliver, 2010; A. Emerick & Reynolds, 2011; Luo & Bhakta, 2020; Evensen et al., 2022).

In this work, we pursue a different (and possibly complementary) approach to improving the prior ensemble by incorporating additional physical knowledge. We thereby consider a situation where the fracture apertures are predominantly created by shearing driven by the tectonic far-field stresses. Toolkits with geomechanical capabilities such as ABAQUS (Smith, 2009; Agheshlui et al., 2018), COMSOL (Multiphysics, 2013), DARTS (Y. Wang et al., 2020; Boersma et al., 2021), ICGT (Thomas et al., 2020; Paluszny et al., 2020), MRST (Ucar et al., 2018; Lie & Møyner, 2021), OpenCSMP (Pezzulli et al., 2022a, 2022b), or XFVM (Deb & Jenny, 2017a, 2017b) can been used to calculate shear displacement and fracture apertures for this scenario. However, it might be computationally expensive to generate a whole ensemble of realisations that are needed as priors for a DA framework, especially when considering a decent number of fractures. A purely stochastic approach on the other hand is unlikely to include all available physical knowledge and cannot represent the complex relationship between apertures and other modal parameters.
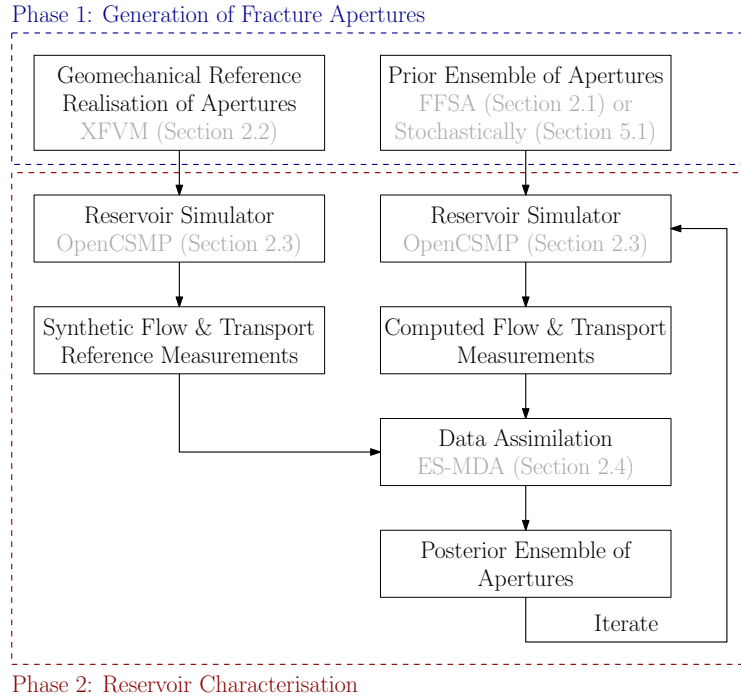
We therefore look for a method that produces physically meaningful prior realisations at little computational cost. For this, we build upon existing proxy models (Milliotte et al., 2018; Agheshlui et al., 2019; J. Wang et al., 2023) and propose a method based on far-field stress approximation (FFSA). FFSA projects the tectonic far-field stresses onto the fracture planes and estimates the shear displacements based on linear elastic theory. Thus, we do not need to solve differential equations, which makes the method computationally attractive. We account for the errors introduced by those approximations by additional uncertainty in a model parameter. We combine the FFSA with the constitutive relations of Barton and Bandis (N. Barton & Choubey, 1977; N. Barton, 1982; Bandis et al., 1983; N. Barton et al., 1985; Lei & Barton, 2022) and integrate it into our ESMDA framework. We use flow and transport data to improve the estimation of the fracture apertures. While a preliminary version of this approach has already been published (Liem et al., 2022), this work refines and extends the method and presents more extensive and impactful results. In particular, we obtain the synthetic reference flow and transport data from a realisation generated with a geomechanical reservoir simulator, and we compare the performance of our DA framework when using prior ensembles generated with the FFSA to two stochastically generated prior ensembles.

This paper is organised as follows: Section 2 introduces our data assimilation framework including the FFSA for generating prior ensembles. In Section 3, we discuss the

fracture geometry, and in Section 4, the model parameters, some of which are assumed to be uncertain. The results of this study, which are presented in Section 5 and discussed in depth in Section 6, show that reasonable prior ensemble realisations can be obtained with FFSA. Ensembles generated with FFSA outperform the ones from two naïve stochastic approaches in our DA framework.

2 Method

In this work, we consider a geological scenario that consists of two phases. In Phase 1, the fracture apertures are generated. We study a thin layer of fractured rock embedded between two impermeable and rigid layers. All fractures are present from the beginning, and we do not consider any fracture propagation. The fractures are initially closed and there is no history of tectonic folding, uplifting, or cooling. We apply a tectonic far-field stress and steadily increase the fluid pressure within the fractures. As the effective normal stress decreases, some fractures begin to slip and consequently dilate due to asperities on the fracture surface. As a result, the apertures vary considerably from fracture to fracture. Due to numerous sources of uncertainty, e.g. in the stress state, rock properties or fracture roughness, the fracture apertures cannot be calculated deterministically but are also associated with some uncertainty. In Phase 2, we perform a tracer test to characterise the reservoir, while we assume that the fluid injection does not affect the fracture apertures. We use an iterative ensemble-based data assimilation (DA) framework (Figure 1) to history match the fracture apertures and obtain a posterior aperture estimate with reduced uncertainty. In the following, the individual building blocks of the DA framework are explained in detail.

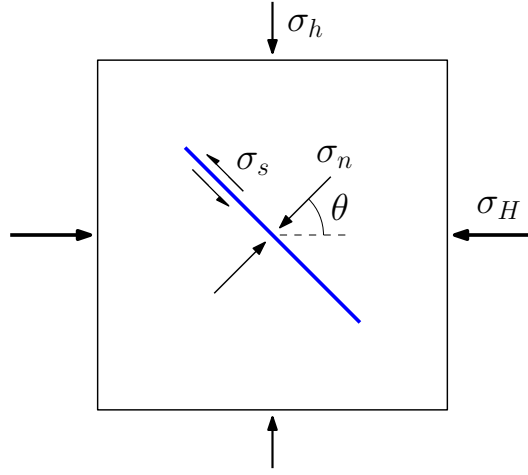**Figure 1.** Iterative data assimilation framework used in this work

2.1 Prior Ensemble of Apertures with Far-Field Stress Approximation (FFSA)

Here, we present a simple and fast method for estimating fracture apertures that can be used to generate a reasonable prior ensemble with little computational cost. We approximate the stress state at the fractures from the far-field stress using Cauchy's equations

$$\sigma_n = \sigma_H \cos^2 \theta + \sigma_h \sin^2 \theta \quad \text{and} \tag{1}$$

$$\sigma_s = (\sigma_h - \sigma_H) \sin \theta \cos \theta \quad , \tag{2}$$

where σ_H and σ_h are the maximum and minimum principal horizontal stresses and θ is the angle between σ_H and the fracture normal (Figure 2). Those equations are only valid for a virtual plane in an intact material, as is the case when all fractures are closed and shear stress is fully transmitted over the fractures. They ignore fracture interactions and hence only provide approximate solutions when shear displacement or tensile opening occurs in other fractures.

Figure 2. Projection of principal horizontal far-field stresses, σ_H and σ_h, onto a fracture

A fracture begins to slip when shear stress exceeds shear strength, i.e. when $|\sigma_s| > \tau_{max}$. The shear strength according to Coulomb's friction law is

$$\tau_{max} = \begin{cases} \sigma_{eff} \cdot \tan(\phi'), & \sigma_{eff} > 0 \\ 0, & \text{otherwise} , \end{cases} \tag{3}$$

where $\sigma_{eff} = \sigma_n - p_f$ is the effective normal stress, ϕ' the friction angle, and p_f the fluid pressure. As the fracture slips, the shear stress relaxes until the arrest criterium

$$|\sigma_s| \leq \tau_{max} \tag{4}$$

is satisfied. We approximate the decrease $\Delta\sigma_s$ in shear stress for an increment $\Delta\delta_s$ of shear displacement with linear elastic theory (Eshelby & Peierls, 1957; Chinnery, 1969; Willis-Richards et al., 1996; Rahman et al., 2002), i.e., we assume

$$\frac{\Delta\sigma_s}{G} = C_g \frac{\Delta\delta_s}{L} , \tag{5}$$

where G is the shear modulus of the surrounding material, L the fracture length and C_g a proportionality factor. This then allows us to calculate the total shear displacement

δ_s of a fracture. The amount of shear dilation δ_d is then obtained by integrating the tangent of the dilation angle ϕ_d over shear displacement, i.e.,

$$\mathrm{d}\delta_d = \mathrm{d}\delta_s \tan(\phi_d) \quad \rightarrow \quad \delta_d = \int_0^{\delta_s} \tan(\phi_d)\, \mathrm{d}\delta_s \,. \tag{6}$$

In this work, we use the constitutive model of Barton and Bandis (N. Barton & Choubey, 1977; N. Barton, 1982; Bandis et al., 1983; N. Barton et al., 1985; Lei & Barton, 2022) to calculate friction and dilation angles (Appendix A1). In this empirical model, these angles are algebraic functions of the shear displacement. They reach a peak value for a certain shear displacement and then decrease for larger displacements. Thus, Equations (3) to (5) form a non-linear system of equations. The fracture aperture

$$a = a_0 - \delta_n + \delta_d \tag{7}$$

is a combination of an initial fracture aperture a_0, closure due to normal stress δ_n and shear dilation δ_d. In this work, we do not consider tensile opening and set the hydraulic aperture equal to the mechanical aperture.

2.2 Geomechanical Reference Realisation of Apertures with XFVM

To generate an accurate reference of the aperture field, we need a proper geomechanical simulator. To this end, we employ an implementation of the extended finite volume method (XFVM), an embedded discrete fracture method that includes lower-dimensional fracture manifolds in Cartesian grids (Deb & Jenny, 2017a, 2017b). In 2D, each fracture is divided into line segments, where each segment has one degree of freedom for shear slip, resulting in piecewise constant displacements along the fractures. Linear elasticity of the rock is assumed, the force balance is solved in an integral manner, and we use Coulomb's friction law (Equation (3)) as a slip criterion. The displacement field is approximated by continuous basis functions at the grid points and discontinuous basis functions to represent fracture manifolds. These special discontinuous basis functions ensure that the displacement gradient is continuous across the manifold, allowing the calculation of shear stress on the fracture without additional constraints. We then solve the system of linear equations for the displacement at the grid points and the shear slip of the segments. As in our approach with FFSA, we calculate shear dilation with the constitutive model of Barton and Bandis described in Appendix A1. To this end, we adjust the dilation angle ϕ_d at each time step to account for changes in roughness while the shear dilation is coupled to the stresses and hence accounted for in the force balance, as described in Conti et al. (2023). The fracture aperture of each segment is obtained from Equation (7), where the initial aperture and normal closure are added in a post-processing step.

2.3 Flow and Transport Computation based on OpenCSMP

As a reservoir simulator, we use the Complex Systems Modelling Platform (OpenCSMP) (Geiger et al., 2004; Matthäi et al., 2007), a finite element – finite volume framework. It offers a wide range of functionality to calculate flow and transport processes with a focus on fractured porous media. In this work, we consider tracer transport by a steady-state velocity field. We calculate the volumetric flow field $\mathbf{q}$ of a single-phase fluid with dynamic viscosity μ through a porous medium with permeability k from Darcy's law

$$\mathbf{q} = -\frac{k}{\mu}\nabla p \tag{8}$$

and the continuity equation $\nabla \cdot \mathbf{q} = \dot{q}_{\text{source}}$, which can be combined and result in the elliptic pressure equation

$$\nabla \cdot \left(\frac{k}{\mu}\nabla p\right) + \dot{q}_{\text{source}} = 0 \,. \tag{9}$$

Here, p is the steady-state pressure and $\dot{q}_{\mathrm{source}}$ is the source term which is positive for fluid injection and negative for extraction. At time t_0, we start injecting a passive tracer which follows the flow field perfectly. The tracer does not alter the flow field and we neglect diffusion. We calculate the evolution of this tracer with the hyperbolic scalar transport equation

$$\phi \frac{\partial c}{\partial t} + \mathbf{q} \cdot \nabla c - \dot{q}_{\mathrm{source}} c_{\mathrm{source}} = 0 \,, \tag{10}$$

where c is the tracer concentration and ϕ the porosity. We solve tracer transport with a first-order version of discrete event simulation (DES) (Shao et al., 2019), a totally asynchronous local time stepping scheme.

2.4 Data Assimilation with ESMDA

In this work, we use the ensemble smoother with multiple data assimilation (ESMDA) proposed by A. A. Emerick and Reynolds (2013). As an ensemble smoother, the ESMDA collects all measurements in time and space in one vector and performs a Kalman update once the reservoir simulation is completed. The ESMDA alternately performs update steps with the same reference measurements and reruns the reservoir simulator with the updated parameters (Figure 1). Those iterations are necessary due to the nonlinear reservoir simulator.

We create a prior ensemble $x_{1:N_E}^{prior}$ of N_E realisations with FFSA and one reference realisation x^{ref} with XFVM. In this work, the parameter vector of a certain realisation i,

$$x_i = \left[\log_{10}(a_1^i), \log_{10}(a_2^i), ..., \log_{10}(a_N^i) \right]^T \,, \tag{11}$$

contains the logarithms of the aperture values of all N fractures. We run a reservoir simulator developed on the basis of OpenCSMP for each realisation to obtain the corresponding measurement vector y_i, which consists of pressure values, volume flow rates and tracer arrival times.

We then get an updated posterior estimation of the fracture apertures with reduced uncertainty by combining the prior knowledge about the model parameter with the uncertainty in the measurements. We thereby integrate the stochastic EnKF of Algorithm 6.3 in Asch et al. (2016) into the ESMDA as described in Liem et al. (2022). The update or analysis step of a standard stochastic EnKF is
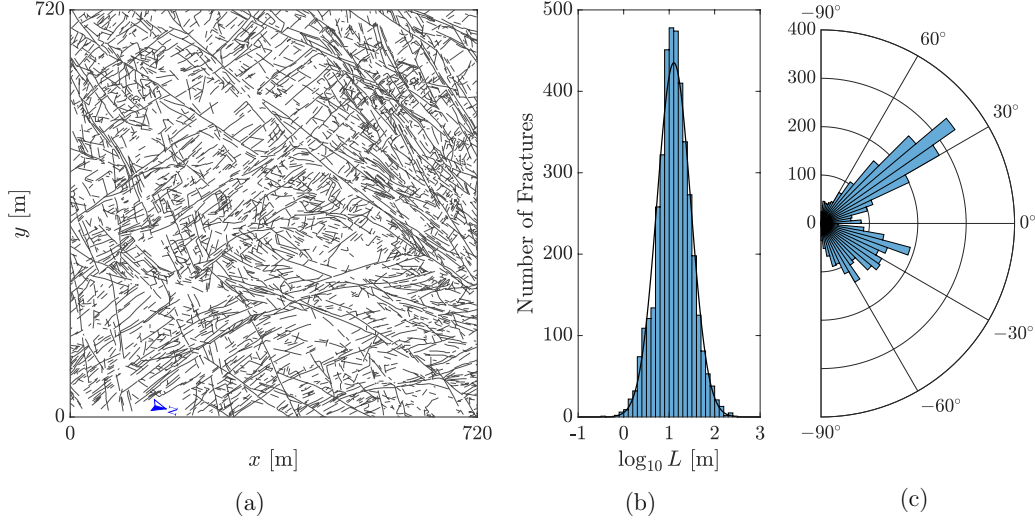
$$x_i^a = x_i^f + K \left(y^{ref} - (y_i + u_i) \right) \qquad \text{with } u_i \sim \mathcal{N}(0, R) \,, \tag{12}$$

where the superscripts f and a denote parameter vectors before and after the update step and the sets of all x_i^f and x_i^a are called prior and posterior ensembles, respectively. R is the measurement error covariance matrix and following van Leeuwen (2020) we apply the perturbations u_i to the ensemble measurements. In order to ensure consistency, the measurement error covariance matrix must be inflated accordingly. This and the calculation of the Kalman gain K are explained in Appendix A2.

3 Fracture Geometry

This study uses a realistic fracture geometry with $N = 4051$ individual fractures (Figure 3a) identical to the one in Liem et al. (2022), except for minor changes in the classification of segments into individual fractures. The geometry was mapped by Odling (1997) from aerial photography of the Hornelen basin in western Norway. The mapped region extends over an area of $720 \times 720\,\mathrm{m}$, with aerial photos taken from a height of $370\,\mathrm{m}$. The smallest observable features were $30\,\mathrm{cm}$ wide depressions filled with soil, grass or water. More fractures became visible at smaller observation heights; thus, the geometry shown in Figure 3a represents merely a subset of the total fractures present.

₃₀₉ The fracture geometry has approximately a log-normal distribution of fracture length
₃₁₀ (Figure 3b) and a bi-modal distribution of fracture orientation with the most prominent
₃₁₁ peak at around 40° (Figure 3c). The Hornelen basin is filled with fractured Devonian-
₃₁₂ age Old Red Sandstone (e.g. Torsvik et al., 1988) with a very low permeability. The frac-
₃₁₃ ture apertures observed at the surface are not representative of the ones at reservoir depth,
₃₁₄ as stress conditions are markedly different. Therefore, we rely on a geomechanical sim-
₃₁₅ ulator to calculate the reference apertures.

Figure 3. Fracture trace map of Hornelen basin outcrop (a) and histogram of logarithm of
fracture length (b) and fracture orientation (c). The line in (b) shows a log-normal distribution
with same mean and standard deviation. The fracture geometry was mapped by Odling (1997)
and digitalised and discretised by Azizmohammadi and Matthäi (2017). Figure adapted from
Liem et al. (2022).

4 Simulation Setup

₃₁₇ The thin horizontal layer of fractured rock is embedded between two rigid and im-
₃₁₈ permeable layers with fractures perpendicular to bedding. These assumptions enable us
₃₁₉ to approximate the model as 2D. We approximate the fractures by straight lines for the
₃₂₀ mechanical simulations (i.e. XFVM and FFSA). For the XFVM reference, we use a grid
₃₂₁ spacing of 2 m, resulting in roughly 46000 fracture segments.

4.1 Uncertain Model Parameters

₃₂₃ While we assume that we know the fracture geometry exactly, other geomechan-
₃₂₄ ical model parameters of Phase 1 are associated with some uncertainty (Table 1). We
₃₂₅ distinguish parameters that are equal for all fractures within one realisation and sam-
₃₂₆ pled therefore only once per realisation (indicated with target 'R') and parameters that
₃₂₇ are different for each fracture within each realisation (target 'F'). Consequently, the to-
₃₂₈ tal number of sampled model parameters per realisation is $8+5N = 20263$. In the fol-
₃₂₉ lowing, we discuss the parameters and their uncertainty in more detail.

₃₃₀ We model a burial depth of the fractured reservoir of 1500 m, corresponding to an
₃₃₁ overburden stress σ_v of approximately 32 MPa based on an average rock density of around
₃₃₂ 2.2 g/cm^3. We assume a normal faulting regime (i.e. $\sigma_v > \sigma_H > \sigma_h$) and set the min-

Table 1. Uncertain geomechanical model parameters. We use scaled beta distributions defined by mean μ, standard deviation σ and [upper bound, lower bound]. For generating the prior ensemble with FFSA, we sample parameters with target 'R' only once per realisation and those with target 'F' for every fracture individually. The last column lists the input parameters for the reference simulation with XFVM.

Symbol	Unit	μ	σ	Bounds	Target	Ref
β	degree	0	5	[-15, 15]	R	0
σ_H	MPa	30	0.6	[28, 32]	R	29.7
σ_h	MPa	23	0.3	[22, 24]	R	23.3
p_f	MPa	21.5	0.15	[21, 22]	R	21.8
ϕ_r	degree	25	1	[22, 28]	R	25
σ_c	MPa	70	3	[61, 79]	R	70
E	MPa	5000	500	[3500, 6500]	R	5000
ν	–	0.25	0.0075	[0.2275, 0.2725]	R	0.25
JRC_{small}	–	6	1	[2, 10]	F	sampled
JRC_{large}	–	2	0.6	[0, 4]	F	sampled
K_{ni}	$\frac{\text{MPa}}{\text{mm}}$	20	5	[10, 30]	F	sampled
v_m^{rel}	–	0.5	0.125	[0.25, 0.75]	F	sampled
C_g	–	1	0.1	[0.7, 1.3]	F	–

imal principal horizontal stress to $\sigma_h \approx 0.7\sigma_v$. The orientation β of the maximum principal horizontal stress σ_H is described in Heidbach et al. (2018); here, we roughly align it to the x-axis of our coordinate system. We assume a constant fluid pressure p_f across the entire field. We choose a fluid pressure close to σ_h to get a reasonable amount of shearing but ensure that it remains smaller than σ_h to prevent tensile opening. Although the material properties of the rock (here Young's modulus E, Poisson's ratio ν, shear modulus $G = \frac{E}{2(1+\nu)}$, unconfined compressive strength σ_c, and residual friction angle ϕ_r) are rarely uniform in a reservoir, we approximate them as such. The chosen values are loosely inspired by Ojo and Brook (1990) and Hawkins and McConnell (1991).

The friction of the fracture planes plays a crucial role and represents a significant source of uncertainty. Two parameters describe friction in our constitutive model (Appendix A1). The residual friction angle ϕ_r is a material property and describes friction of a planar rock surface. The joint roughness coefficient JRC, on the other hand, describes the increase of friction due to surface roughness which differs from fracture to fracture. In this work, we consider surface roughness at two different length scales: small-scale roughness at the level of the asperities (e.g. Pollard & Aydin, 1988) as described by the original Barton and Bandis model and modelled here with JRC_{small}, and an additional roughness compensating for idealising fractures as straight lines in our model. We calculate the combined joint roughness coefficient as

$$JRC = JRC_{small} + JRC_{large} \cdot \log_{10}(L) \, , \tag{13}$$

where the fracture length L is in meters.

Additional fracture parameters in the Barton and Bandis model (Appendix A1) include the initial normal stiffness K_{ni} and the maximum possible closure $v_m = v_m^{rel} a_0$. While the FFSA provides accurate results for a single fracture, it does not account for interactions between fractures (Appendix A3). To address the limitations of this approximation, we introduce additional uncertainty through the proportionality coefficient C_g that relates shear stress to shear displacement.

The amount of shear displacement and consequently also fracture aperture obtained from FFSA corresponds to the maximum value along the fracture length. In the frictionless case, shear displacement follows an elliptic profile (Eshelby & Peierls, 1957). Due to the non-linear constitutive model of Barton and Bandis, the profiles of shear displacement and aperture are only approximately elliptic. Those profiles can have in general arbitrary shapes in the XFVM. For simplicity, however, we assume a constant aperture over the length of a fracture and assign it to the maximum aperture value.

Ideally, we would compare the FFSA prior to a prior ensemble generated from XFVM. However, this is computationally too expensive. We therefore compare it to prior ensembles from two naïve stochastic approaches. They both sample from the unconditional probability density function (PDF) of the FFSA prior.

4.2 Parameters for Flow and Transport Simulation and ESMDA Updates

In Phase 2 of the geological scenario, we alternately perform tracer tests and update the fracture apertures with ESMDA. For the tracer test, we inject fluid through a single fracture named 'well fracture', which is located at the centre of the domain, and apply a constant pressure at all four boundaries (Figure 4a). Starting at time $t_0 = 0$, a scalar tracer with concentration $c = 1$ is introduced into the injected fluid. We compute the steady-state velocity field and tracer transport using OpenCSMP (Section 2.3). The matrix domain is thereby discretised with an unstructured triangular mesh, and the fractures are represented as lower-dimensional line elements (Azizmohammadi & Matthäi, 2017). In this work, we decouple flow and transport from the fracture mechanics, assuming that fluid injection does not affect the fracture apertures. While this assumption is often invalid in real-world scenarios, it is necessary in our framework due to computational limitations. The relevant parameters for the flow and transport simulations are provided in Table 2. Note that we calculate the fracture permeabilities from the fracture apertures assuming plane Poiseuille flow between two parallel plates.

Table 2. Parameters for flow and transport simulation with OpenCSMP

Fluid viscosity	μ	$1 \times 10^{-3}\,\mathrm{Pa\,s}$
Matrix permeability	k_m	$3 \times 10^{-13}\,\mathrm{m}^2$
Matrix porosity	ϕ_m	0.15
Fracture permeability	k_f	$a^2/12$
Fracture porosity	ϕ_f	1.0
Pressure at all 4 boundaries	p_{out}	$9\,\mathrm{MPa}$
Inlet volume flow	$\dot{Q}_{\mathrm{in}}/l_w$	$2 \times 10^{-3}\,\mathrm{m}^2/\mathrm{s}$
Length of well fracture	l_w	$56.48\,\mathrm{m}$
CFL multiplier for DES		0.4

In this work, we assume that measurements along the domain boundary and in the well fracture are available (Figure 4b). Concretely, we measure the maximum value of the steady-state pressure p_{in} along the well fracture and the volume flow rate $\dot{Q}_{\mathrm{out}}$ through 20 model-boundray segments. Further, we monitor the evolution of the tracer concen-

tration at certain locations on the boundary and either use the concentration value after 320 days, c_{320}, or the time it takes to reach a concentration of 0.5, $t_{0.5}$, as measurements. The number of measurements and their locations are arbitrary choices. To evaluate the performance of the DA framework, we set 12 measurements (indicated in yellow in Figure 4b) aside and use the remaining 60 measurements for the ESMDA updates. We call them test and training measurements, respectively. We scale the measurements as

$$\tilde{p}_{\mathrm{in}} = \frac{p_{\mathrm{in}} - p_{\mathrm{out}}}{p_{\mathrm{out}}} \quad , \quad \tilde{\dot{Q}}_{\mathrm{out}}^{(i)} = \frac{\dot{Q}_{\mathrm{out}}^{(i)}}{\dot{Q}_{\mathrm{in}}/20} \quad , \quad \tilde{t}_{0.5}^{(i)} = \frac{t_{0.5}^{(i)}}{640\,\mathrm{days}} \quad , \quad \tilde{c}_{320}^{(i)} = c_{320}^{(i)} \qquad (14)$$

and collect them in the training and test measurement vectors

$$y = \left[\tilde{p}_{\mathrm{in}} \,,\, \tilde{\dot{Q}}_{\mathrm{out}}^{(1)} \,,\, ... \,,\, \tilde{\dot{Q}}_{\mathrm{out}}^{(16)} \,,\, \tilde{t}_{0.5}^{(1)} \,,\, ... \,,\, \tilde{t}_{0.5}^{(19)} \,,\, \tilde{c}_{320}^{(1)} \,,\, ... \,,\, \tilde{c}_{320}^{(24)}\right]^T \text{ and} \qquad (15)$$

$$z = \left[\tilde{\dot{Q}}_{\mathrm{out}}^{(17)} \,,\, ... \,,\, \tilde{\dot{Q}}_{\mathrm{out}}^{(20)} \,,\, \tilde{t}_{0.5}^{(20)} \,,\, ... \,,\, \tilde{t}_{0.5}^{(25)} \,,\, \tilde{c}_{320}^{(25)} \,,\, ... \,,\, \tilde{c}_{320}^{(26)}\right]^T \,, \qquad (16)$$

respectively. The superscript (i) denotes individual measurements of a certain quantity.

Figure 4. Boundary conditions for the flow and transport simulations (a) and location of measurements for ESMDA updates (b). The labels M1-2 and T1-2 mark specific training and test locations, respectively.

After obtaining those measurements for every realisation, we update the parameter vectors containing the logarithm of all 4051 fracture aperture values using ESMDA. For the scaled dimensionless measurements we assume a diagonal error covariance matrix R with each element of the diagonal set to 1×10^{-5}. In this work, we do not apply any covariance localisation or inflation. We study the influence of ensemble size N_E and the number of ESMDA iterations N_{iter} on the results of the DA framework. For a quantitative evaluation, we utilise the mean root-mean-square error defined as

$$\text{M-RMSE}_\xi = \frac{1}{N_\xi} \sum_{i=1}^{N_\xi} \sqrt{\frac{1}{N_E} \sum_{j=1}^{N_E} \left(\xi_i^{(j)} - \xi_i^{(ref)}\right)^2} \,, \qquad (17)$$
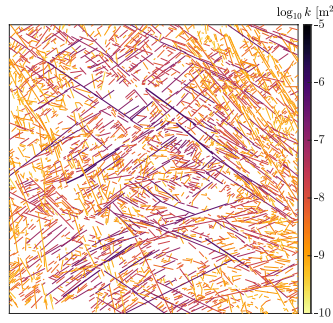
where ξ can represent either the log-apertures x, training measurements y, or test measurement z. Here, $\xi_i^{(j)}$ denotes the i-th entry in the corresponding vector of the j-th realisation, and N_ξ refers to the length of that vector.

5 Results

In this section, we first analyse the prior ensemble obtained from FFSA by comparing it to the reference realisation from XFVM as well as to two prior ensembles from the naïve stochastic approaches. Subsequently, we show that the prior ensemble from FFSA outperforms the stochastic approaches in our DA framework.
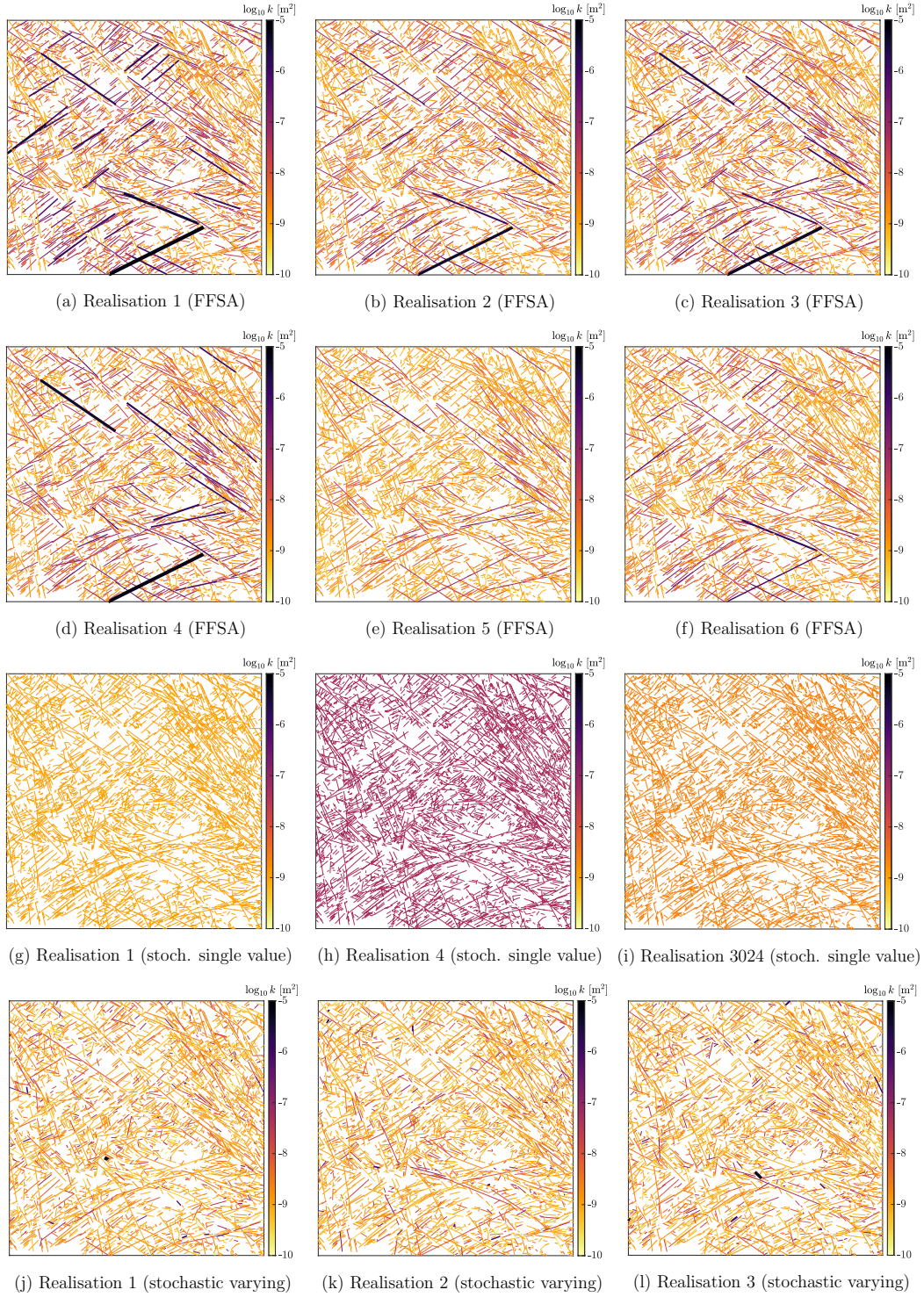
5.1 Prior ensemble

We first compare the maximum aperture value of each fracture. The reference realisation obtained with XFVM is shown in Figure 5 and realisations 1 to 6 of the prior ensemble generated with FFSA are depicted in Figures 6a–f, each obtained from a different set of sampled model parameter values. The realisations of the FFSA prior have a notable variability which reflects the uncertainty in the model parameters as defined in Table 1. Although none of the 6 prior realisations are particularly close to the reference, they nevertheless capture trends and features of it.
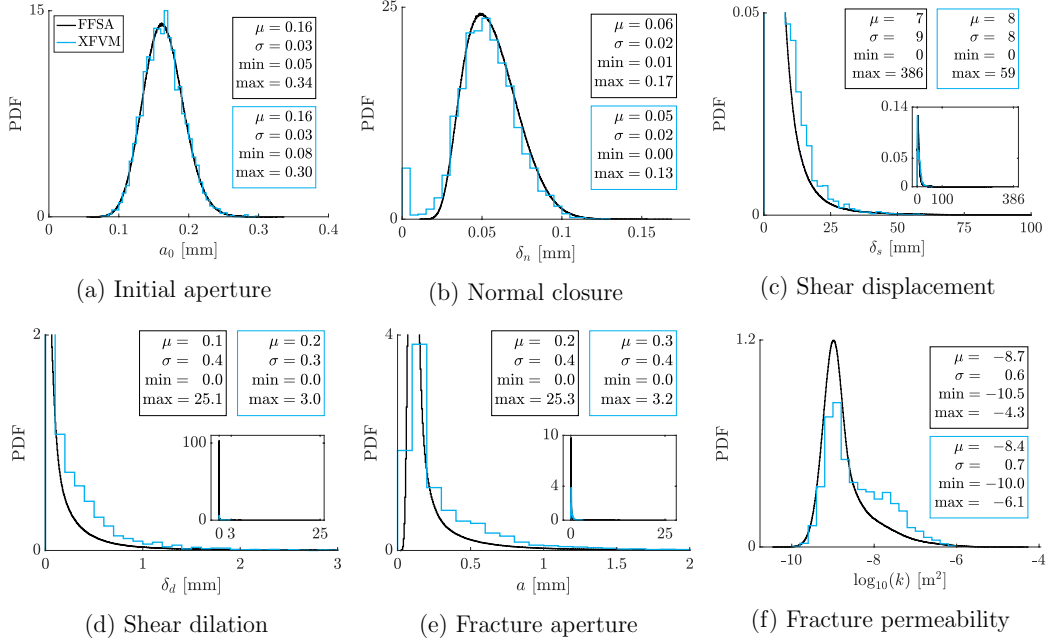

Figure 5. Reference realisation with XFVM. Line thickness corresponds to aperture width and line colour to $\log_{10}$ of the fracture permeability.

From the prior ensemble with FFSA, we extract the unconditional PDF of the apertures and related quantities from all fractures in all realisations (black curves in Figure 7). The corresponding PDF from the reference simulation is shown in blue. Overall the two curves in Figure 7 agree very well, although there are distinct differences. Firstly and most notably, the FFSA prior underestimates the number of fractures with moderate fracture permeability in the range of $10^{-8}\,\mathrm{m^2}$ to $10^{-7}\,\mathrm{m^2}$ (Figure 7f). We attribute this to the slightly smaller mean shear displacement (Figure 7c) which we believe is a consequence of neglecting fracture interactions. Secondly, the maximum values of shear displacement and subsequently also aperture are significantly higher in the FFSA prior than in the XFVM reference (Figure 7c). This occurs when very small friction and C_g values are sampled for long and favourably oriented fractures in the FFSA prior. Such extreme values are not present in the parameter set of the reference. Lastly, fracture interaction can modify the local stress field, resulting in situations where the effective normal stress can become small or even negative. Therefore, some fractures in the XFVM reference experience little to no normal closure (Figure 7b). In contrast, all fractures in the FFSA prior have positive effective normal stress and consequently some amount of normal closure, as fracture interaction is neglected there. Even with these differences, we expect the ensemble generated with FFSA to be a suitable prior for our DA framework.

We aim to compare the FFSA prior to two prior ensembles from naïve stochastic approaches. For the first approach, named here stochastic single value prior, we sample one value per realisation from the unconditional PDF of the FFSA prior (i.e. black curve in Figure 7e) and set all apertures in that realisation to this value. For the second ap-

(a) Realisation 1 (FFSA) (b) Realisation 2 (FFSA) (c) Realisation 3 (FFSA)

(d) Realisation 4 (FFSA) (e) Realisation 5 (FFSA) (f) Realisation 6 (FFSA)

(g) Realisation 1 (stoch. single value) (h) Realisation 4 (stoch. single value) (i) Realisation 3024 (stoch. single value)

(j) Realisation 1 (stochastic varying) (k) Realisation 2 (stochastic varying) (l) Realisation 3 (stochastic varying)

Figure 6. Realisations of the prior ensemble with FFSA (a–f), stochastic single value (g–i) and stochastic varying (j–l). Line thickness corresponds to aperture width and line colour to $\log_{10}$ of the fracture permeability.

Figure 7. Combined histogram of the values of all 4051 fractures in 5000 realisations with FFSA (black) and the reference simulation with XFVM (blue)

proach, named stochastic varying prior, we independently sample aperture values for every fracture in every realisation from the same PDF. Figures 6g–l show realisations of those two prior ensembles. Visually, the FFSA prior is much closer to the reference than the stochastic ones, even though all three prior ensembles follow the same unconditional PDF.

5.2 Posterior ensemble

Now we want to investigate how the three different prior ensembles perform in our DA framework. We first analyse the measurements and then the apertures of the posterior ensembles.

We monitor the evolution of the tracer concentration over time at specific locations on the boundary of the domain (Figure 4b). Figure 8 shows the resulting breakthrough curves at two training and two test locations for three prior ensembles of different sizes generated with FFSA and corresponding posterior ensembles. At the training locations, either a concentration or arrival time measurement is taken for the ESMDA update, whereas at test locations, the breakthrough curve measurement is solely used for evaluating the performance of ESMDA but not in the update itself. The breakthrough curves of the prior ensembles have a considerable spread at all four locations as a result of the uncertain fracture apertures. At training locations, the posterior ensembles closely match the reference realisation from XFVM. We obtain a good match of the entire breakthrough curves even though only a single concentration or arrival time measurement per location is used. In test locations, the level of uncertainty is only slightly reduced, and a considerable spread remains in the posterior ensembles. With the FFSA prior we get essentially converged results already for an ensemble size of 500, as the results remain consistent for larger ensemble sizes.
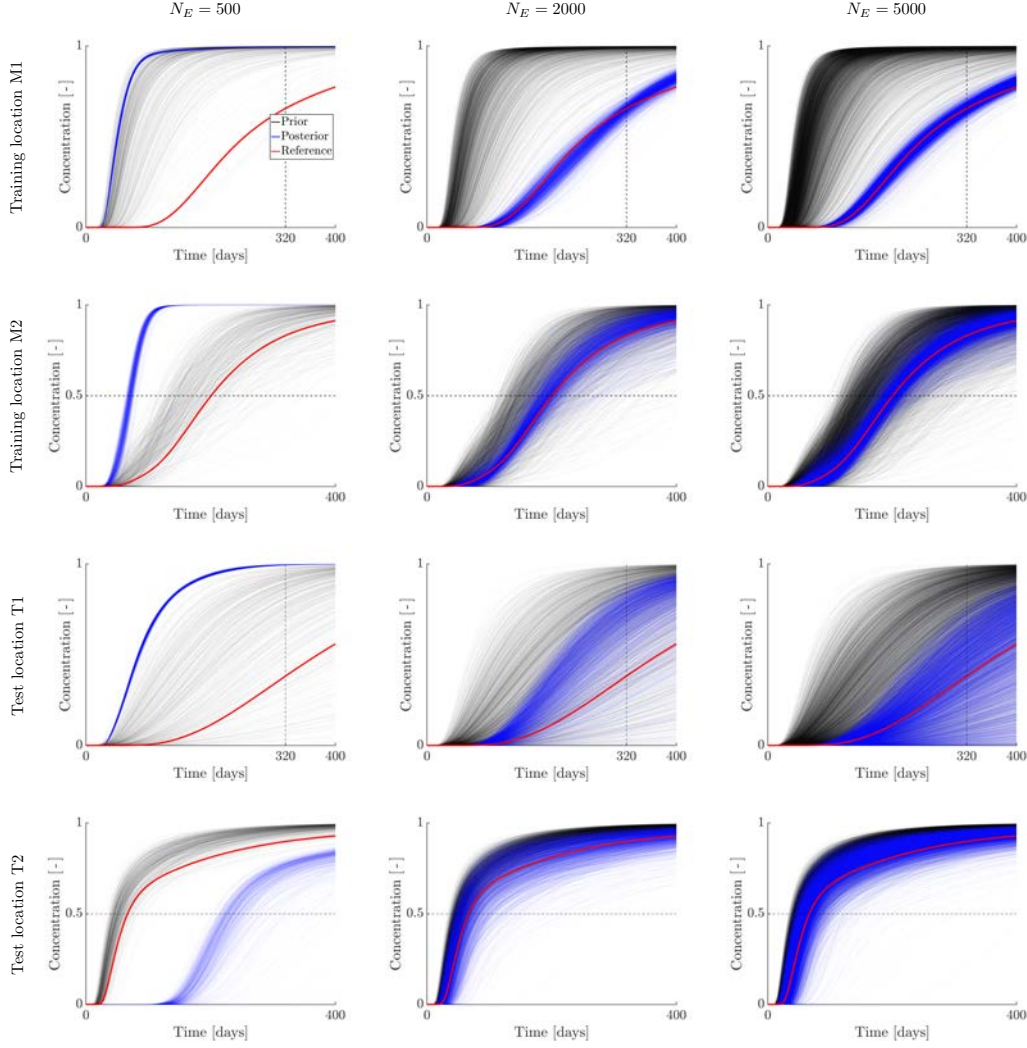
The same breakthrough curves for the stochastic varying prior are shown in Figure 9. Here, the posterior of the smallest ensemble size (i.e., with $N_E = 500$) collapsed

Figure 8. Breakthrough curves of the FFSA prior. The prior ensemble is in black, the posterior ensemble in blue and the XFVM reference in red. The locations of two training and two test locations are indicated in Figure 4. The columns correspond to different ensemble sizes and the dashed lines indicate the measurements.

and converged to a wrong solution. Results with larger ensemble sizes are generally fine; however, test location T1 indicates that $N_E = 2000$ is not large enough for full convergence regarding ensemble size. Compared to the FFSA prior, the ensemble spread is larger for the stochastic varying prior, both in the prior ensembles and consequently also in the posterior ensembles.
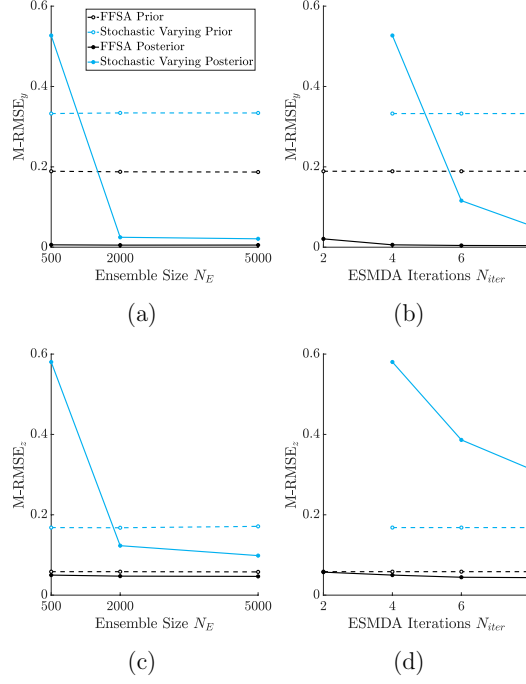
We quantify the performance of the FFSA and stochastic varying priors with the mean root-mean-square error of the training and test measurements, as defined in Equation (17), for different ensemble sizes and numbers of ESMDA iterations (Figure 10a–d). Comparing the FFSA posterior to its prior, we see that the error in the training measurements is drastically reduced, while the error in the test measurements is only slightly smaller. An ensemble size of 500 and 4 ESMDA iterations is sufficient to achieve satisfactory results for the FFSA prior. For the stochastic varying prior however, a combination of ensemble size and number of ESMDA iterations beyond our computational ca-

Figure 9. Breakthrough curves of the stochastic varying prior. The prior ensemble is in black, the posterior ensemble in blue and the XFVM reference in red. The locations of two training and two test locations are indicated in Figure 4. The columns correspond to different ensemble sizes and the dashed lines indicate the measurements.

pabilities is required for converged results. Compared to FFSA, the training and test errors of the stochastic varying prior are 1.8 and 3.0 times larger, respectively. For the combination with the smallest errors (i.e., with $N_E = 5000$ and $N_{iter} = 4$), the corresponding ratios in the posterior are 3.9 and 2.1. In short, the results from the FFSA prior match the measurements better than the ones from the stochastic varying prior, but the latter also produces a posterior with substantially reduced measurement errors, given a sufficiently large ensemble size.

A significant difference exists between the updated fracture apertures obtained with the two methods. Figure 11 shows some realisations of the posterior ensembles obtained from the FFSA and stochastic varying priors for $N_E = 5000$ and $N_{iter} = 4$. Generally, the posterior realisations of FFSA (Figure 11a–f) are more similar to the reference than the corresponding realisations from the prior ensemble (Figure 6a–f), and the variability of the realisations in the ensemble is reduced. For example, realisations 5 and 6
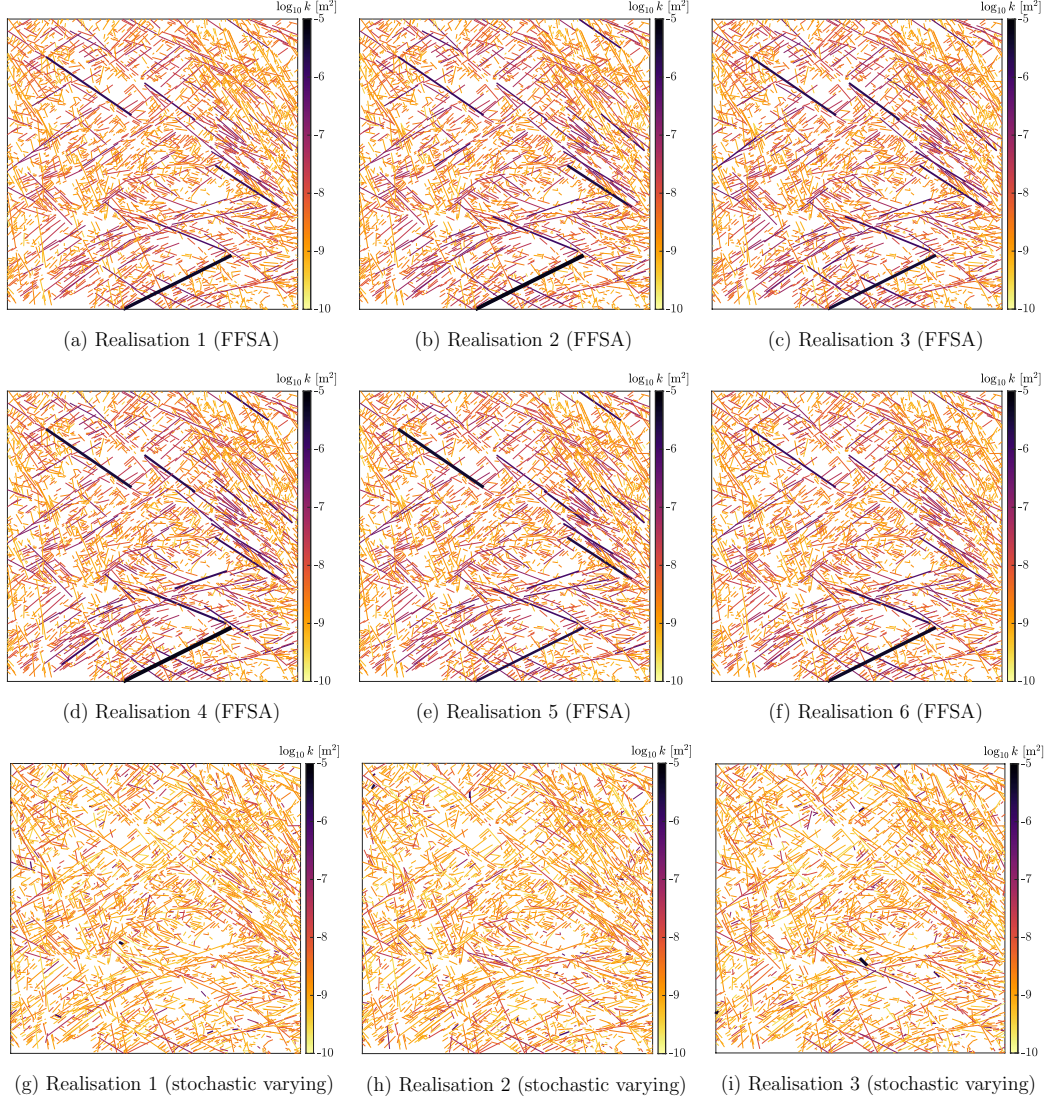
Figure 10. Mean root-mean-square error (M-RMSE) of training (a, b) and test (c, d) measurements calculated with Equation (17). Figures (a, c) show results for $N_{iter} = 4$ and (b, d) for $N_E = 500$.

show overall increased apertures, and the apertures of the prominent long fractures are slightly reduced in realisation 1. However, the posterior realisations are not an exact match to the reference, as the apertures of long and optimally oriented fractures are still overestimated, while the ones of many short fractures are underestimated. These qualitative observations are supported by Figure 12a, which shows a slight improvement in the unconditional PDF of the FFSA posterior compared to the prior. Conversely, the posterior realisations of the stochastic varying priors (Figure 11g–i) appear to be almost identical to the corresponding prior realisations (Figure 6j–l), and only fractures near measurement locations are visibly improved. The corresponding unconditional PDF shows extreme minimum and maximum permeability values which reach unphysical levels. The mean root-mean-square errors of the log-apertures (Figure 12b–c) show a marginal improvement for FFSA but no improvement for the stochastic varying prior. The drastic increase in the posterior errors for the stochastic varying prior arises from an ensemble collapse to a wrong solution.
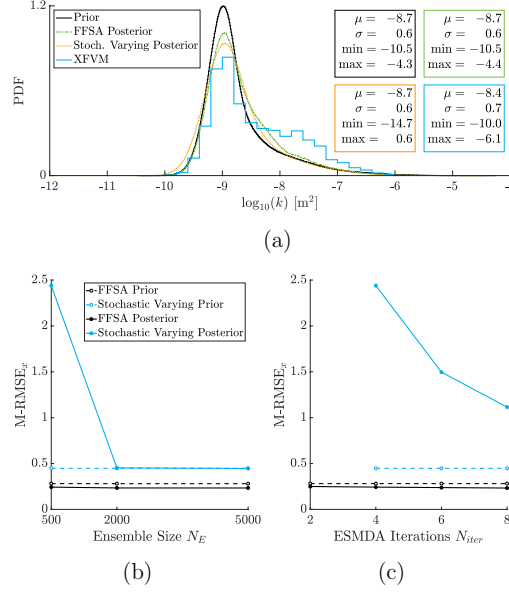
The stochastic single value prior fails to produce satisfactory results in the DA framework, leading to ensemble collapse regardless of the ensemble size and number of ESMDA iterations. In light of this, we calculate the root-mean-square error of the training measurements for each prior realisation as

$$\text{RMSE}_y^{(j)} = \sqrt{\frac{1}{N_y} \sum_{i=1}^{N_y} \left(y_i^{(j)} - y_i^{(ref)} \right)^2} \tag{18}$$

and find the one with the smallest error (Figure 13a). The best realisation has an aperture of 0.16 mm and is shown in Figure 6i. Although some breakthrough curves obtained from this realisation show somewhat acceptable agreement with the reference (Figure 13c), others display substantial errors (Figure 13b). As expected, it is therefore not possible

(a) Realisation 1 (FFSA) (b) Realisation 2 (FFSA) (c) Realisation 3 (FFSA)

(d) Realisation 4 (FFSA) (e) Realisation 5 (FFSA) (f) Realisation 6 (FFSA)

(g) Realisation 1 (stochastic varying) (h) Realisation 2 (stochastic varying) (i) Realisation 3 (stochastic varying)
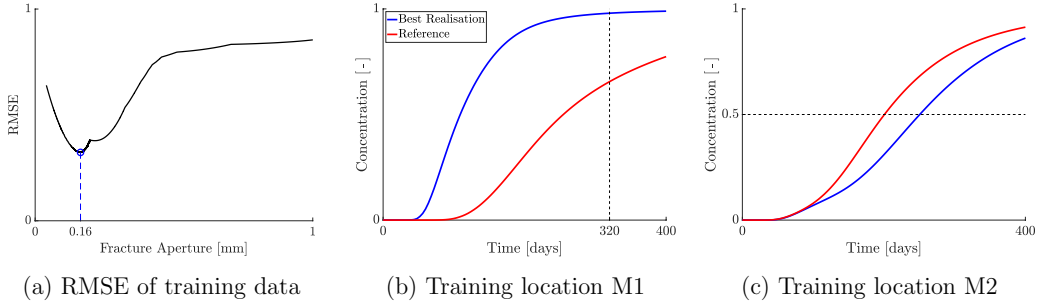
Figure 11. Realisations of the posterior ensemble obtained from the FFSA prior (a–f) and the stochastic varying prior (g–i) for $N_E = 5000$ and $N_{iter} = 4$. Line thickness corresponds to aperture width and line colour to $\log_{10}$ of the fracture permeability.

Figure 12. Combined histogram of fracture permeability values of all 4051 fractures for $N_E = 5000$ and $N_{iter} = 4$ (a) and mean root-mean-square error (M-RMSE) of log-apertures calculated with Equation (17) for $N_{iter} = 4$ (b) and $N_E = 500$ (c)

to match the complex flow and transport behaviour of the reference when using only a single value for all fracture apertures.

(a) RMSE of training data   (b) Training location M1   (c) Training location M2

Figure 13. Root-mean-square error (RMSE) of the training data for the stochastic single value prior shows that the realisation with a fracture aperture of $0.16\,\text{mm}$ has the smallest error (a). Breakthrough curves at two locations as indicated in Figure 4 for this best realisation in blue and the XFVM reference in red (b, c).

6 Discussion

The FFSA provides reasonable approximations of the fracture apertures in a scenario dominated by shear dilation. It is thereby substantially faster than a geomechanical simulator like XFVM. For the presented fracture model, the FFSA takes less than a minute while the XFVM runs for several days. However, neither code is fully optimised for speed, and there is potential to significantly improve the computational efficiency of XFVM. The speed of FFSA makes it an attractive option for generating prior ensem-

bles for DA purposes, as typically a large number of realisations is required. In contrast, using geomechanical simulators for this task might become computationally prohibitive.

The FFSA is only exact for a single isolated fracture with constant friction angle and it neglects fracture interactions. This leads to modelling errors (see Appendix A3 for a direct comparison to XFVM), particularly as shearing of a fracture can change the local stress field considerably. To compensate for those errors, we introduce additional uncertainty through the parameter C_g, a proportionality factor between shear stress and shear displacement. While this approach gives overall satisfactory results, moderate fracture permeabilities are under-represented in the PDF of the FFSA prior ensemble compared to the one of the reference realisation obtained with XFVM (Figure 7f), indicating that the chosen approach is not yet optimal.

With the current approach, the fracture length has a much larger influence on the shear displacement than the parameter C_g because the uncertainty in C_g is much smaller than the variation of the fracture length in our model (Equation (5)). Increasing the uncertainty in C_g would however lead to more extreme values for long fractures. Therefore, an improved approach should increase the probability of moderate apertures for short fractures without generating extremely high apertures for long fractures. For example, we could model the uncertainty of C_g as a function of fracture length or introduce an additive uncertainty directly to the fracture aperture in Equation (7). Another approach is adding additional uncertainty to the stress state, thereby modelling the change in the local stress state at one fracture due to the shearing of other fractures. Further, we could improve the FFSA itself by incorporating knowledge of the surrounding fracture geometry or using a hierarchical approach, i.e., first estimating shear displacement and apertures of the large fractures, and then deriving the local stress field at the smaller ones.

Even without the above-mentioned improvements, the FFSA produces prior realisations that are much closer to the reference than the two naïve stochastic approaches. Subsequently, the FFSA prior also leads to a better posterior ensemble than the stochastic approaches. We can state that, at least in our setting, a better prior leads to a better posterior and it is therefore crucial to model the prior appropriately.

In this work, we confirm that it is not possible to retrieve the complex flow and transport behaviour of the reference when using only a single value for all fracture apertures. Even when the optimal single aperture is used, the resulting realisation still has a considerable error in the measurements, leading to completely wrong estimates of some breakthrough curves (Figure 13). The stochastic single value prior led to an ensemble collapse in our DA framework irrespective of the ensemble size. We believe this collapse results from a combination of factors. Firstly, the relations between the single aperture value and certain measurements become constant above or below specific thresholds, resulting in a loss of ensemble variation for those measurements and, in extreme cases, an identical measurement value for all realisations. Secondly, some of those relations exhibit non-monotonic behaviour such that realisations can be attracted by non-optimal local minima. Thirdly, the stochastic single value prior generates realisations confined to a limited subset with highly correlated measurements, leading to numerical issues when calculating the Kalman gain (Equation (A8) in Appendix A2). Lastly, one reference measurement lies entirely outside the range of the prior ensemble. Consequently, we were unable to obtain any DA results for this prior.

While the stochastic single value prior is too restrictive, the stochastic varying prior bears too much uncertainty. It does not incorporate all available knowledge, such as correlations of fracture aperture with length and orientation. As a consequence, a large ensemble size is required to avoid undersampling. In this study, undersized ensembles collapsed and converged to wrong solutions. Results suggest that a smaller ensemble size might be possible with more ESMDA iterations, but the required combination of ensemble size and number of ESMDA iterations is beyond our current computational capabil-

ities, and thus, our results with this prior are not fully converged. Nevertheless, we expect that results with a much larger ensemble size are similar to the ones from our best combination ($N_E = 5000$, $N_{iter} = 4$). With this combination, we obtain a posterior ensemble that matches the training measurements, i.e., measurements that are used for the ESMDA update, quite well. The improvement in the test measurements, which are solely used for evaluating the outcome of the DA framework, is smaller and a considerable amount of uncertainty remains. The apertures of the posterior realisations differ however significantly from the reference realisation, with updates predominantly occurring near measurement locations. This emphasises the importance of considering more than just the (training) measurements when evaluating the effectiveness of a DA framework.

With the FFSA prior, we obtain posterior realisations with an improved estimation of the apertures compared to the ones from the prior ensemble, even though a considerable difference to the reference realisation remains. The posterior ensemble matches the training measurements of the reference realisation very well, while the test measurements are only marginally improved, indicating that the improvements in flow and transport are mostly limited to the vicinity of training measurements. More measurements, especially also from the interior of the domain, are needed to further improve the estimation of aperture as well as the flow and transport. However, the number of measurement locations already exceeds what one can expect in field studies and a complete observation of flow and transport is only possible in lab experiments such as e.g. in Flemisch et al. (2023). While there is room for improvement, the posterior from the FFSA prior gives good estimates of the fracture apertures, which can be used for performance estimation and risk assessment in subsurface applications. Concrete examples involve optimal placement of boreholes for injection or extraction, expected heat extraction in a geothermal reservoir, or preventing potential contamination of nearby aquifers.

Our results, especially the ones with the stochastic varying prior, suggest that most apertures only have a negligible influence on the measurements at the boundaries. While this is expected to some degree, we also identify three constraints in our study setup that artificially limit the influence of the fractures. Firstly, we use a first-order transport scheme which leads to a considerable amount of numerical diffusion. Diffusion smears out the concentration front and thus dampens the effects of the fractures. We could avoid this by using a higher-order scheme and only include a controlled amount of physical diffusion. Secondly, the sensitivity of the fracture apertures on the flow and transport measurements is highly dependent on the ratio of matrix to fracture permeability (Phillips, 1991; Matthäi & Belayneh, 2004). In cases with very low matrix permeability, the flow is governed by the fracture topology, favouring flow paths with minimal matrix distances. In this regime, fracture aperture influences flow only when equivalent flow paths exist. Conversely, in cases with very high matrix permeability, flow predominantly occurs within the matrix, largely independent of fracture parameters. Only in the intermediate range of matrix permeabilities do the fracture apertures have a significant influence on flow and transport. We have not optimised the matrix permeability for maximum sensitivity of the apertures, as it is not a tuning parameter in practical scenarios. Lastly, boundary conditions might contribute to these limitations as well. By imposing a fixed pressure on the domain's boundary, we disregard that the fractured rock typically extends beyond the region of interest. Flow and transport near the boundary are strongly influenced by the boundary condition. Alternative approaches, such as implementing infinite boundary conditions or using measurements only in the interior of the domain, might decrease the influence of the boundary conditions on the measurements and represent real-world conditions more accurately.

Nevertheless, the posterior from the FFSA prior also shows slightly improved apertures in the interior of the domain. In such priors, apertures of fractures with similar length and orientation are correlated. Hence, fractures in the interior of the domain are corre-

lated to measurements through similar fractures near the measurement locations and therefore also updated by ESMDA. In reality, apertures are correlated with length and orientation (C. A. Barton et al., 1995; Baghbanan & Jing, 2008; N. Barton & Quadros, 2015; X. Zhang et al., 2021), and such indirect updates are desired to some extent. However, the current implementation of the FFSA prior overestimates these correlations, leading to a posterior with deficient variability. We expect that these issues can be resolved by the above-mentioned improvements of FFSA.

In this study, we used a geological scenario where the generation of the fracture apertures occurs before the reservoir characterisation with the tracer test. However, injecting fluid into the reservoir during the tracer test alters the effective normal stresses at the fractures and consequently fracture aperture, which in turn affects the flow field. In future works, it is therefore desirable to couple flow and mechanics and consider poroelasticity. A further step towards a more realistic setting is the extension to 3D, which is straightforward for FFSA. The far-field stresses can be projected onto the fracture planes with a 3D version of Equations (1) and (2), and the process of approximating the maximum shear displacement is similar to that in 2D. For that purpose, Chinnery (1969) lists values of the proportionality factor C_g for various fracture shapes. Special attention must be given to the definition of fracture length, however. In future works, we could also consider additional model parameters as uncertain, such as matrix permeability and porosity, and allow for uncertainties in the boundary conditions of the tracer test. Here, we consider rock properties as spatially homogeneous, but we could also model them with e.g. Gaussian random fields as in Liem et al. (2022).

Arguably the biggest assumption in this work is that we know the fracture geometry (i.e., location, orientation and length of each fracture) *a priori* and exactly. In reality, the fracture geometry is usually associated with substantial uncertainty, as only sparse borehole data and statistical information are available. Nevertheless, valuable insight is obtained from this study, as discussed above. We see this study as a necessary intermediate step towards a more realistic setup that eventually also includes uncertain fracture geometry. Several existing tools can be used or built upon to generate physically meaningful realisations of a fracture geometry, e.g. as in Hyman et al. (2015), Lei et al. (2017), Gläser et al. (2020), and Paluszny et al. (2020). It should then be straightforward to update input parameters of the fracture generator (such as statistics of e.g. fracture length or density). It is however very challenging to update the actual fracture geometry itself. Parametrising the generated fracture geometry efficiently and effectively for this purpose is complex as the number of fractures can vary between realisations, and a fracture from one realisation generally does not have a bijectively related fracture in other realisations. Existing approaches based on level set function or Hough transform (Ping et al., 2017; Chai et al., 2018; Yao et al., 2018), to our knowledge, have not been applied to complex large fracture geometries yet. The task becomes even more challenging if the parameterisation should also reflect relations between fractures, including fractures terminating against other fractures and formation history. Additionally, automatic remeshing of the updated fracture geometry might be challenging as arbitrary small distances or angles may occur. For this purpose, non-conforming discretisation as in the embedded discrete fracture model (EDFM) is beneficial.

7 Conclusion

In this work, we suggest using the far-field stress approximation (FFSA), a proxy model designed to estimate fracture apertures in shear-dominated scenarios, to generate prior ensembles for data assimilation (DA). The FFSA captures the general trends effectively, albeit with some inherent errors due to neglecting fracture interactions. We use FFSA to generate realistic and computationally efficient prior ensembles for ensemble-based data assimilation. To compensate for modelling errors, we introduce supplementary uncertainty in one model parameter. Comparing FFSA priors to those from two naïve

stochastic approaches reveals notable differences. While all methods share the same underlying unconditional PDF, FFSA-derived realisations are much closer to the reference realisation from a geomechanical simulator.

Employing ESMDA, we update fracture apertures with flow and transport data. The posterior ensemble obtained from the FFSA prior matches the flow and transport behaviour as well as the apertures, although some differences remain. In contrast, the posterior ensemble obtained from an unconditional sampling of the apertures (i.e., a stochastic varying prior) yields apertures that substantially deviate from the reference despite matching training measurements. In addition, a significantly larger ensemble size is required than for the FFSA prior, increasing overall computational cost. The third prior, which uses the same value for all fracture apertures in a realisation, cannot match the complex flow and transport behaviour of our synthetic reference. Our results show a correlation between the prior and posterior uncertainties and highlight the importance of a good estimation of the prior ensemble. We expect that those results also apply to other ensemble-based DA methods, for example particle filters.

While the current form of FFSA already produces reasonable results, opportunities for improvement, particularly in addressing modelling errors through additional uncertainties, remain. To achieve this, we plan to conduct a more detailed study with the FFSA in a separate work. Further potential improvements for the ESMDA framework include constructing a prior ensemble that combines realisations from different methods and the use of adaptive localisation. Moreover, we aim to make the framework more realistic by coupling flow and transport with mechanics, incorporating additional physics like heat transport, and eventually accounting for uncertainty in fracture geometry.

Appendix A Appendix

A1 Fracture Aperture Model of Barton and Bandis

In this work, we use the constitutive model of Barton and Bandis (N. Barton & Choubey, 1977; N. Barton, 1982; Bandis et al., 1983; N. Barton et al., 1985) where the aperture of a fracture a is a combination of the initial aperture a_0, closure due to normal stress δ_n and dilation due to shearing δ_d (Equation (7)).

The initial aperture

$$a_0 = \frac{JRC}{5}\left(0.2\frac{\sigma_c}{JCS} - 0.1\right) \tag{A1}$$

corresponds to the fracture aperture under stress-free conditions. It is a function of the (peak) joint roughness coefficient JRC and the amount of joint alteration described by the ratio of unconfined compressive strength of the rock σ_c and joint wall compression strength JCS. In this work, we assume that the fractures are unaltered and unweathered (i.e. $JCS = \sigma_c$), and therefore the initial aperture depends on the surface roughness only.

Assuming a positive effective normal stress $\sigma_{eff} > 0$, the amount of closure is

$$\delta_n = \frac{\sigma_{eff}v_m}{K_{ni}v_m + \sigma_{eff}} \ , \tag{A2}$$

where v_m and K_{ni} are the maximum possible closure and the initial normal stiffness, respectively. Under increasing normal stress, more and more asperities are in contact and consequently, the normal stiffness of the fracture increases. The model of Barton and Bandis is not applicable if fluid pressure exceeds normal stress (i.e. for negative σ_{eff}) and tensile opening occurs.

A key feature of the model of Barton and Bandis is that the friction angle

$$\phi' = JRC_{mob}\log_{10}\left(\frac{JCS}{\sigma_{eff}}\right) + \phi_r \tag{A3}$$

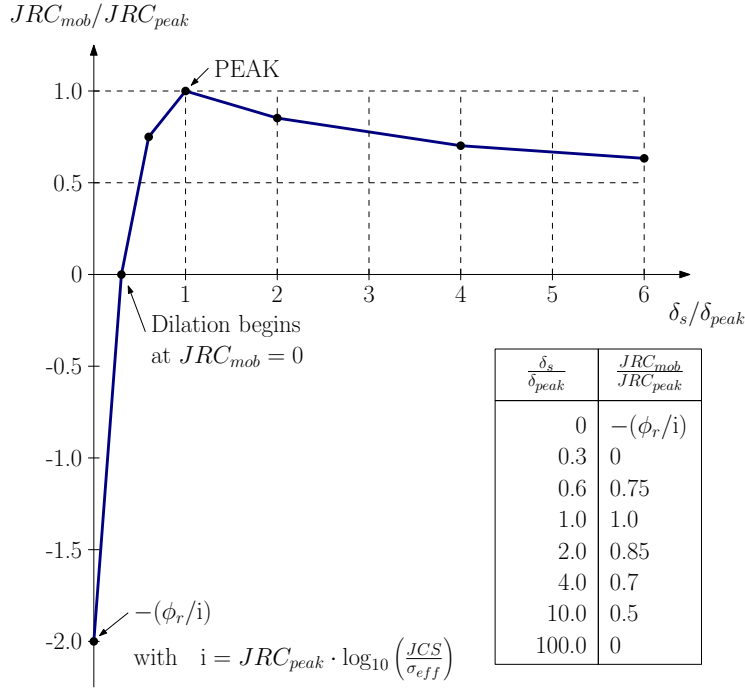737 and dilation angle

$$\phi_d = \frac{1}{M}(\phi' - \phi_r) = \frac{1}{M} JRC_{mob} \log_{10}\left(\frac{JCS}{\sigma_{eff}}\right) \tag{A4}$$

739 are not constant but vary with the amount of shear displacement. This dependency is
740 modelled with the mobilised joint roughness coefficient JRC_{mob} (Figure A1). The peak
741 shear displacement δ_{peak} corresponds to the amount of shearing when peak shear strength
742 is reached. Here, we use

$$\delta_{peak} = 0.0077 L^{0.45} \left(\frac{\sigma_{eff}}{JCS}\right)^{0.34} \cos\left(JRC \cdot \log_{10}\left(\frac{JCS}{\sigma_{eff}}\right)\right) , \tag{A5}$$

744 as proposed by Asadollahi and Tonon (2010). For pre-peak shearing ($\delta_s < \delta_{peak}$), the
745 degradation of the few asperities that are in contact increases the interlocking between
746 the two fracture surfaces and consequently increases the friction. For post-peak shear-
747 ing ($\delta_s > \delta_{peak}$) on the other hand, roughness is getting destroyed and smoothed out.
748 Subsequently, shear strength and dilation angle are steadily reduced. For an infinite amount
749 of shearing, the friction angle is equal to the residual friction angle and the dilation an-
750 gle approaches zero.

Figure A1. Mobilised joint roughness coefficient JRC_{mob} as a function of shear displacement δ_s. Figure reproduced from Liem et al. (2022), original figure from N. Barton (1982) and N. Barton et al. (1985).

751 For the damage coefficient M in Equation (A3) we use the formula proposed by
752 N. Barton and Choubey (1977)

$$M = 0.7 + JRC \Big/ \left[12 \log_{10}\left(\frac{JCS}{\sigma_{eff}}\right)\right] . \tag{A6}$$

754 In this work, we neglect the decrease in aperture for small shear displacements and there-
755 fore integrate only over positive dilation angles in Equation (6). The model of Barton

and Bandis has been developed for fractures with a constant fluid pressure and thus a relatively constant effective normal stress. In our simulation however, the fluid pressure is steadily increased and the effective normal stress might become very small in some fractures or even locally negative for some segments in the reference simulation with XFVM. We therefore approximate σ_{eff} in Equations (A3) to (A6) as

$$\sigma_{eff} \approx \sigma_n - \frac{1}{2}\left(\frac{|\sigma_s|}{\tan\phi_r} + p_f^{end}\right) , \tag{A7}$$

where we calculate σ_n and σ_s with Cauchy's equations (Equations (1) to (2)) and p_f^{end} is the target fluid pressure.

A2 Details of ESMDA

In Equation (12), we use a stochastic version of the Kalman update in the ESMDA. Following Asch et al. (2016), we approximate the Kalman gain

$$K = P^f H^T \left[HP^f H^T + R\right]^{-1} \simeq X^f\left(Y^f\right)^T\left[Y^f\left(Y^f\right)^T\right]^{-1} \tag{A8}$$

with the normalised anomalies

$$\left[X^f\right]_i = \frac{1}{\sqrt{N_E - 1}}\left(x_i^f - \frac{1}{N_E}\sum_{j=1}^{N} x_j^f\right) \quad \text{and} \tag{A9}$$

$$\left[Y^f\right]_i = \frac{1}{\sqrt{N_E - 1}}\left(\left(y_i^f + u_i\right) - \frac{1}{N_E}\sum_{j=1}^{N}\left(y_j^f + u_j\right)\right) . \tag{A10}$$

Here, P^f is the forecast error covariance matrix and H the linearised version of the observation operator $\mathcal{H}(.)$, which maps the input vector x_i to the measurement vector y_i.

In order to guarantee a correct posterior distribution in a linear model with Gaussian error statistics, the ESMDA inflates the measurement error covariance matrix R in Equation (12), i.e.,

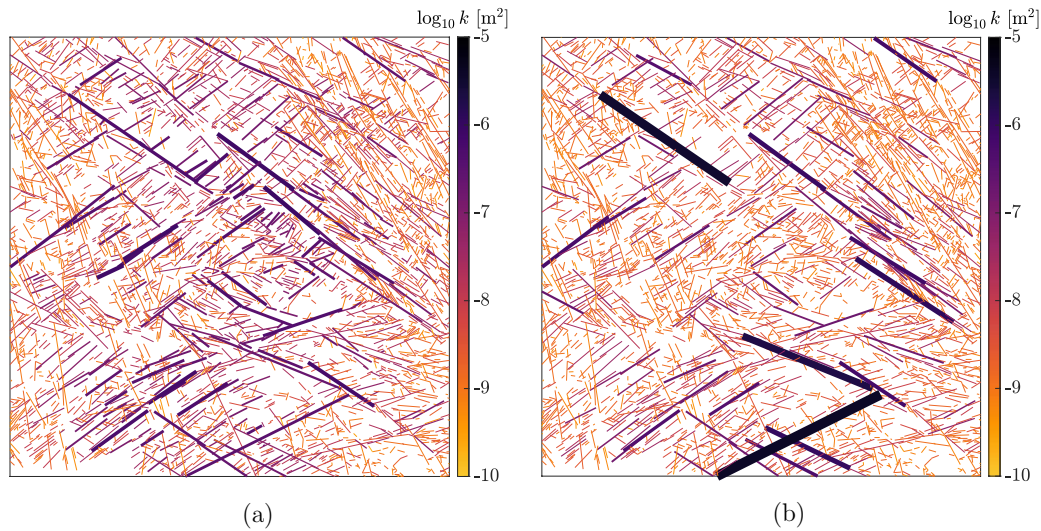$$\widetilde{R}_m = \alpha_m R \quad \text{such that} \quad \sum_{m=1}^{M}\frac{1}{\alpha_m} = 1 , \tag{A11}$$

where M is the number of ESMDA iterations (A. A. Emerick & Reynolds, 2013). In this study, we use a constant inflation factor $\alpha_m = M \ \forall m$.

A3 Comparison of XFVM and FFSA

Figure A2 shows the results of XFVM and FFSA for the exact same underlying model parameters (i.e. the values from the last column of Table 1) and $C_g = 1$. The FFSA captures the general trends and some apertures agree quite well. However, there are also quite large differences for many fractures. Most notably, the apertures of long, optimally oriented fractures are overestimated while the apertures of some short fractures are underestimated. We intend to compare those two methods thoroughly in a separate publication.

Open Research Section

MATLAB scripts of the far-field stress approximation (FFSA), the ANSYS mesh of the fracture geometry, input and output files of the reference simulation with extended finite volume method (XFVM), and prior and posterior ensembles of the data assimilation framework based on the ensemble smoother with multiple data assimilation (ESMDA) are available at ETH Zurich via `https://doi.org/10.3929/ethz-b-000632502` (Liem et al., 2023).

Figure A2. Results with XFVM (a) and FFSA (b) for the same underlying model parameters. Line thickness corresponds to aperture width and line colour to $\log_{10}$ of the fracture permeability.

References

Agheshlui, H., Sedaghat, M. H., & Azizmohammadi, S. (2019). A comparative study of stress influence on fracture apertures in fragmented rocks [Journal Article]. *Journal of Rock Mechanics and Geotechnical Engineering*, *11*(1), 38-45. doi: 10.1016/j.jrmge.2018.05.003

Agheshlui, H., Sedaghat, M. H., & Matthai, S. (2018). Stress influence on fracture aperture and permeability of fragmented rocks [Journal Article]. *Journal of Geophysical Research: Solid Earth*, *123*(5), 3578-3592. doi: 10.1029/2017JB015365

Ahr, W. M. (2008). *Geology of carbonate reservoirs: the identification, description and characterization of hydrocarbon reservoirs in carbonate rocks* [Book]. Hoboken: John Wiley & Sons. doi: DOI:10.1002/9780470370650

Al-Dhafeeri, A. M., & Nasr-El-Din, H. A. (2007). Characteristics of high-permeability zones using core analysis, and production logging data [Journal Article]. *Journal of Petroleum Science and Engineering*, *55*(1), 18-36. doi: 10.1016/j.petrol.2006.04.019

Ali, M. Y., Bouchaala, F., Bouzidi, Y., Takam Takougang, E. M., Mohamed, A. A. I., & Sultan, A. (2021). Integrated fracture characterization of thamama reservoirs in abu dhabi oil field, united arab emirates [Journal Article]. *SPE Reservoir Evaluation & Engineering*, *24*(04), 708-720. doi: 10.2118/206737-PA

Amann, F., Gischig, V., Evans, K., Doetsch, J., Jalali, R., Valley, B., . . . Giardini, D. (2018). The seismo-hydromechanical behavior during deep geothermal

reservoir stimulations: open questions tackled in a decameter-scale in situ stimulation experiment [Journal Article]. *Solid Earth*, *9*(1), 115-137. doi: 10.5194/se-9-115-2018

Anderson, J. L., & Anderson, S. L. (1999). A monte carlo implementation of the nonlinear filtering problem to produce ensemble assimilations and forecasts [Journal Article]. *Monthly Weather Review*, *127*(12), 2741-2758. doi: 10.1175/1520-0493(1999)127⟨2741:AMCIOT⟩2.0.CO;2

Asadollahi, P., & Tonon, F. (2010). Constitutive model for rock fractures: Revisiting barton's empirical model [Journal Article]. *Engineering Geology*, *113*(1), 11-32. doi: 10.1016/j.enggeo.2010.01.007

Asch, M., Bocquet, M., & Nodet, M. (2016). *Data assimilation: Methods, algorithms, and applications* [Book Section]. Philadelphia: Society for Industrial and Applied Mathematics. doi: 10.1137/1.9781611974546.ch6

Azizmohammadi, S., & Matthäi, S. K. (2017). Is the permeability of naturally fractured rocks scale dependent? [Journal Article]. *Water Resources Research*, *53*(9), 8041-8063. doi: 10.1002/2016WR019764

Baghbanan, A., & Jing, L. (2008). Stress effects on permeability in a fractured rock mass with correlated fracture length and aperture [Journal Article]. *International Journal of Rock Mechanics and Mining Sciences*, *45*(8), 1320-1334. doi: 10.1016/j.ijrmms.2008.01.015

Bandis, S. C., Lumsden, A. C., & Barton, N. R. (1983). Fundamentals of rock joint deformation [Journal Article]. *International Journal of Rock Mechanics and Mining Sciences & Geomechanics Abstracts*, *20*(6), 249-268. doi: 10.1016/0148-9062(83)90595-8

Bannister, R. N. (2017). A review of operational methods of variational and ensemble-variational data assimilation [Journal Article]. *Quarterly Journal of the Royal Meteorological Society*, *143*(703), 607-633. doi: 10.1002/qj.2982

Barton, C. A., Zoback, M. D., & Moos, D. (1995). Fluid flow along potentially active faults in crystalline rock [Journal Article]. *Geology*, *23*(8), 683-686. doi: 10.1130/0091-7613(1995)023⟨0683:FFAPAF⟩2.3.CO;2

Barton, N. (1982). *Modelling rock joint behavior from in situ block tests: implications for nuclear waste repository design* (Vol. 308) [Book]. Columbus: Office of Nuclear Waste Isolation, Battelle Project Management Division.

Barton, N., Bandis, S., & Bakhtar, K. (1985). Strength, deformation and conductivity coupling of rock joints [Journal Article]. *International Journal of Rock Mechanics and Mining Sciences & Geomechanics Abstracts*, *22*(3), 121-140. doi: 10.1016/0148-9062(85)93227-9

Barton, N., & Choubey, V. (1977). The shear strength of rock joints in theory and practice [Journal Article]. *Rock mechanics*, *10*(1), 1-54. doi: 10.1007/BF01261801

Barton, N., & Quadros, E. (2015). Anisotropy is everywhere, to see, to measure, and to model [Journal Article]. *Rock Mechanics and Rock Engineering*, *48*(4), 1323-1339. doi: 10.1007/s00603-014-0632-7

Bear, J., & Cheng, A. H. D. (2010). *Modeling groundwater flow and contaminant transport* (Vol. 23) [Book]. Dordrecht: Springer.

Boersma, Q. D., Bruna, P. O., de Hoop, S., Vinci, F., Moradi Tehrani, A., & Bertotti, G. (2021). The impact of natural fractures on heat extraction from tight triassic sandstones in the west netherlands basin: a case study combining well, seismic and numerical data [Journal Article]. *Netherlands Journal of Geosciences*, *100*, e6. doi: 10.1017/njg.2020.21

Bui, M., Adjiman, C. S., Bardow, A., Anthony, E. J., Boston, A., Brown, S., . . . Mac Dowell, N. (2018). Carbon capture and storage (ccs): the way forward [Journal Article]. *Energy & Environmental Science*, *11*(5), 1062-1176. doi: 10.1039/C7EE02342A

Carrassi, A., Bocquet, M., Bertino, L., & Evensen, G. (2018). Data assimilation

in the geosciences: An overview of methods, issues, and perspectives [Journal Article]. *WIREs Climate Change*, *9*(5), e535. doi: doi.org/10.1002/wcc.535

Casini, G., Hunt, D. W., Monsen, E., & Bounaim, A. (2016). Fracture characterization and modeling from virtual outcrops [Journal Article]. *AAPG Bulletin*, *100*(1), 41-61. doi: 10.1306/09141514228

Chai, Z., Tang, H., He, Y., Killough, J., & Wang, Y. (2018). Uncertainty quantification of the fracture network with a novel fractured reservoir forward model [Conference Proceedings]. In *Spe annual technical conference and exhibition* (p. 19). SPE: Society of Petroleum Engineers. doi: 10.2118/191395-MS

Chen, Y., & Oliver, D. S. (2010). Cross-covariances and localization for enkf in multiphase flow data assimilation [Journal Article]. *Computational Geosciences*, *14*(4), 579-601. doi: 10.1007/s10596-009-9174-6

Chen, Y., & Oliver, D. S. (2012). Ensemble randomized maximum likelihood method as an iterative ensemble smoother [Journal Article]. *Mathematical Geosciences*, *44*(1), 1-26. doi: 10.1007/s11004-011-9376-z

Chen, Y., & Oliver, D. S. (2013). Levenberg–marquardt forms of the iterative ensemble smoother for efficient history matching and uncertainty quantification [Journal Article]. *Computational Geosciences*, *17*(4), 689-703. doi: 10.1007/s10596-013-9351-5

Chilès, J.-P., & Delfiner, P. (2012). *Geostatistics : modeling spatial uncertainty* (2nd ed. ed.) [Book]. Hoboken, N.J: Wiley.

Chinnery, M. A. (1969). Theoretical fault models [Conference Proceedings]. In K. Kasahara & A. Stevens (Eds.), *A symposium on processes in the focal region* (Vol. 37, p. 211-223). Ottawa: Publ. Dominion Obs. doi: doi.org/10.4095/315467

Conti, G., Matthäi, S., & Jenny, P. (2023). XFVM modelling of fracture aperture induced by shear and tensile opening [Journal Article]. *Computational Geosciences*. doi: 10.1007/s10596-023-10214-5

Deb, R., & Jenny, P. (2017a). Finite volume–based modeling of flow-induced shear failure along fracture manifolds [Journal Article]. *International Journal for Numerical and Analytical Methods in Geomechanics*, *41*(18), 1922-1942. doi: doi.org/10.1002/nag.2707

Deb, R., & Jenny, P. (2017b). Modeling of shear failure in fractured reservoirs with a porous matrix [Journal Article]. *Computational Geosciences*, *21*(5), 1119-1134. doi: 10.1007/s10596-017-9680-x

Emerick, A., & Reynolds, A. (2011). Combining sensitivities and prior information for covariance localization in the ensemble kalman filter for petroleum reservoir applications [Journal Article]. *Computational Geosciences*, *15*(2), 251-269. doi: 10.1007/s10596-010-9198-y

Emerick, A. A., & Reynolds, A. C. (2013). Ensemble smoother with multiple data assimilation [Journal Article]. *Computers & Geosciences*, *55*, 3-15. doi: 10.1016/j.cageo.2012.03.011

Eshelby, J. D., & Peierls, R. E. (1957). The determination of the elastic field of an ellipsoidal inclusion, and related problems [Journal Article]. *Proceedings of the Royal Society of London. Series A. Mathematical and Physical Sciences*, *241*(1226), 376-396. Retrieved from `doi.org/10.1098/rspa.1957.0133` doi: 10.1098/rspa.1957.0133

Evensen, G. (1994). Sequential data assimilation with a nonlinear quasi-geostrophic model using monte carlo methods to forecast error statistics [Journal Article]. *Journal of Geophysical Research: Oceans*, *99*(C5), 10143-10162. doi: 10.1029/94JC00572

Evensen, G. (2003). The ensemble kalman filter: theoretical formulation and practical implementation [Journal Article]. *Ocean Dynamics*, *53*(4), 343-367. doi: 10.1007/s10236-003-0036-9

Evensen, G., Vossepoel, F. C., & van Leeuwen, P. J. (2022). *Data assimilation*

fundamentals: A unified formulation of the state and parameter estimation problem [Book]. Cham: Springer Nature.

Flemisch, B., Nordbotten, J. M., Fernø, M., Juanes, R., Class, H., Delshad, M., ... Zhang, Z. (2023). *The fluidflower international benchmark study: Process, modeling results, and comparison to experimental data.* doi: 10.48550/arXiv.2302.10986

Flury, M., Flühler, H., Jury, W. A., & Leuenberger, J. (1994). Susceptibility of soils to preferential flow of water: A field study [Journal Article]. *Water Resources Research, 30*(7), 1945-1954. doi: 10.1029/94WR00871

Geiger, S., Cortis, A., & Birkholzer, J. T. (2010). Upscaling solute transport in naturally fractured porous media with the continuous time random walk method [Journal Article]. *Water Resources Research, 46*(12). doi: 10.1029/2010WR009133

Geiger, S., Roberts, S., Matthäi, S. K., Zoppou, C., & Burri, A. (2004). Combining finite element and finite volume methods for efficient multiphase flow simulations in highly heterogeneous and structurally complex geologic media [Journal Article]. *Geofluids, 4*(4), 284-299. doi: 10.1111/j.1468-8123.2004.00093.x

Genter, A., Castaing, C., Dezayes, C., Tenzer, H., Traineau, H., & Villemin, T. (1997). Comparative analysis of direct (core) and indirect (borehole imaging tools) collection of fracture data in the hot dry rock soultz reservoir (france) [Journal Article]. *Journal of Geophysical Research: Solid Earth, 102*(B7), 15419-15431. doi: 10.1029/97JB00626

Gläser, D., Flemisch, B., Class, H., & Helmig, R. (2020). Frackit: a framework for stochastic fracture network generation and analysis [Journal Article]. *Journal of Open Source Software, 5*(56), 2291. doi: 10.21105/joss.02291

Gutmanis, J., Ardèvol i Oró, L., Díez-Canseco, D., Chebbihi, L., Awdal, A., & Cook, A. (2018). Fracture analysis of outcrop analogues to support modelling of the subseismic domain in carbonate reservoirs, south-central pyrenees [Journal Article]. *Geological Society, London, Special Publications, 459*(1), 139-156. Retrieved from `doi.org/10.1144/SP459.2` doi: 10.1144/SP459.2

Hawkins, A., & McConnell, B. J. (1991). Influence of geology on geomechanical properties of sandstones [Conference Proceedings]. In *7th isrm congress* (p. ISRM-7CONGRESS-1991-051). Aachen, Germany: OnePetro. Retrieved from `https://onepetro.org/isrmcongress/proceedings-abstract/CONGRESS91/All-CONGRESS91/ISRM-7CONGRESS-1991-051/167521`

Heidbach, O., Rajabi, M., Cui, X., Fuchs, K., Müller, B., Reinecker, J., ... Zoback, M. (2018). The world stress map database release 2016: Crustal stress pattern across scales [Journal Article]. *Tectonophysics, 744*, 484-498. doi: doi.org/10.1016/j.tecto.2018.07.007

Houtekamer, P. L., & Mitchell, H. L. (2001). A sequential ensemble kalman filter for atmospheric data assimilation [Journal Article]. *Monthly Weather Review, 129*(1), 123-137. doi: 10.1175/1520-0493(2001)129⟨0123:ASEKFF⟩2.0.CO;2

Houtekamer, P. L., & Zhang, F. (2016). Review of the ensemble kalman filter for atmospheric data assimilation [Journal Article]. *Monthly Weather Review, 144*(12), 4489-4532. doi: 10.1175/MWR-D-15-0440.1

Hyman, J. D., Karra, S., Makedonska, N., Gable, C. W., Painter, S. L., & Viswanathan, H. S. (2015). dfnworks: A discrete fracture network framework for modeling subsurface flow and transport [Journal Article]. *Computers & Geosciences, 84*, 10-19. doi: 10.1016/j.cageo.2015.08.001

Häring, M. O., Schanz, U., Ladner, F., & Dyer, B. C. (2008). Characterisation of the basel 1 enhanced geothermal system [Journal Article]. *Geothermics, 37*(5), 469-495. doi: 10.1016/j.geothermics.2008.06.002

Johnston, P. B., Atkinson, T. C., Odling, N. E., & Barker, J. A. (2005). Models of tracer breakthrough and permeability in simple fractured porous media [Journal Article]. *Geological Society, London, Special Publications, 249*(1), 91-102.

doi: 10.1144/GSL.SP.2005.249.01.08

Kalman, R. E. (1960). A new approach to linear filtering and prediction problems [Journal Article]. *Journal of Basic Engineering*, *82*(1), 35-45. doi: 10.1115/1.3662552

Keller, J., Hendricks Franssen, H.-J., & Marquart, G. (2018). Comparing seven variants of the ensemble kalman filter: How many synthetic experiments are needed? [Journal Article]. *Water Resources Research*, *0*(0). doi: 10.1029/2018WR023374

Kumagai, N., Tanaka, T., & Kitao, K. (2004). Characterization of geothermal fluid flows at sumikawa geothermal area, japan, using two types of tracers and an improved multi-path model [Journal Article]. *Geothermics*, *33*(3), 257-275. doi: 10.1016/j.geothermics.2003.08.010

Lei, Q., & Barton, N. (2022). On the selection of joint constitutive models for geomechanics simulation of fractured rocks [Journal Article]. *Computers and Geotechnics*, *145*, 104707. doi: 10.1016/j.compgeo.2022.104707

Lei, Q., Latham, J.-P., & Tsang, C.-F. (2017). The use of discrete fracture networks for modelling coupled geomechanical and hydrological behaviour of fractured rocks [Journal Article]. *Computers and Geotechnics*, *85*, 151-176. doi: 10.1016/j.compgeo.2016.12.024

Lie, K., & Møyner, O. (Eds.). (2021). *Advanced modeling with the matlab reservoir simulation toolbox* [Book]. Cambridge: Cambridge University Press. doi: 10.1017/9781009019781

Liem, M., Conti, G., Matthai, S. K., & Jenny, P. (2023). *Data collection: Prior with far-field stress approximation for ensemble-based data assimilation in naturally fractured reservoirs* [Data Collection]. ETH Zurich. doi: 10.3929/ethz-b-000632502

Liem, M., & Jenny, P. (2020). Two-stage ensemble kalman filter approach for data assimilation applied to flow in fractured media [Conference Proceedings]. In *Ecmor 2022* (Vol. 2020, p. 1-14). doi: 10.3997/2214-4609.202035126

Liem, M., Matthai, S. K., & Jenny, P. (2022). Estimation of fracture aperture in naturally fractured reservoirs using an ensemble smoother with multiple data assimilation [Conference Proceedings]. In *Ecmor 2022* (Vol. 2022, p. 1-18). doi: 10.3997/2214-4609.202244068

Liu, E., & Martinez, A. (2012). *Seismic fracture characterization* (E. Liu & A. Martinez, Eds.) [Book Section]. Oxford: EAGE. Retrieved from https://www.sciencedirect.com/science/article/pii/B9789073834408500140

Liu, Q., Xue, L., Sarout, J., Lin, Q., Pan, W., Liu, Y., & Feng, R. (2022). Automatic history matching of multistage fractured shale gas reservoir constrained by microseismic data [Journal Article]. *Journal of Petroleum Science and Engineering*, *213*, 110357. doi: doi.org/10.1016/j.petrol.2022.110357

Lu, J., Kordi, M., Hovorka, S. D., Meckel, T. A., & Christopher, C. A. (2013). Reservoir characterization and complications for trapping mechanisms at cranfield co2 injection site [Journal Article]. *International Journal of Greenhouse Gas Control*, *18*, 361-374. doi: doi.org/10.1016/j.ijggc.2012.10.007

Luo, X., & Bhakta, T. (2020). Automatic and adaptive localization for ensemble-based history matching [Journal Article]. *Journal of Petroleum Science and Engineering*, *184*, 106559. doi: 10.1016/j.petrol.2019.106559

Matthäi, S. K., & Belayneh, M. (2004). Fluid flow partitioning between fractures and a permeable rock matrix [Journal Article]. *Geophysical Research Letters*, *31*(7). doi: 10.1029/2003GL019027

Matthäi, S. K., Geiger, S., Roberts, S. G., Paluszny, A., Belayneh, M., Burri, A., ... Heinrich, C. A. (2007). Numerical simulation of multi-phase fluid flow in structurally complex reservoirs [Journal Article]. *Geological Society, London, Special Publications*, *292*(1), 405. doi: 10.1144/SP292.22

Milliotte, C., Jonoud, S., Wennberg, O. P., Matthäi, S. K., Jurkiw, A., & Mosser, L.

(2018). Well-data-based discrete fracture and matrix modelling and flow-based upscaling of multilayer carbonate reservoir horizons [Journal Article]. *Geological Society, London, Special Publications*, *459*(1), 191. doi: 10.1144/SP459.7

Multiphysics, C. (2013). Comsol multiphysics reference manual [Journal Article]. *COMSOL: Grenoble, France*, *1084*, 834.

Odling, N. E. (1997). Scaling and connectivity of joint systems in sandstones from western norway [Journal Article]. *Journal of Structural Geology*, *19*(10), 1257-1271. doi: 10.1016/S0191-8141(97)00041-2

Ojo, O., & Brook, N. (1990). The effect of moisture on some mechanical properties of rock [Journal Article]. *Mining Science and Technology*, *10*(2), 145-156. doi: 10.1016/0167-9031(90)90158-O

Paluszny, A., Thomas, R. N., Saceanu, M. C., & Zimmerman, R. W. (2020). Hydro-mechanical interaction effects and channelling in three-dimensional fracture networks undergoing growth and nucleation [Journal Article]. *Journal of Rock Mechanics and Geotechnical Engineering*, *12*(4), 707-719. Retrieved from https://www.sciencedirect.com/science/article/pii/S167477552030072X doi: https://doi.org/10.1016/j.jrmge.2020.04.004

Parker, J. C. (1989). Multiphase flow and transport in porous media [Journal Article]. *Reviews of Geophysics*, *27*(3), 311-328. doi: 10.1029/RG027i003p00311

Pezzulli, E., Nejati, M., Salimzadeh, S., Matthäi, S. K., & Driesner, T. (2022a). An enhanced j-integral for hydraulic fracture mechanics [Journal Article]. *International Journal for Numerical and Analytical Methods in Geomechanics*, *46*(11), 2163-2190. doi: 10.1002/nag.3383

Pezzulli, E., Nejati, M., Salimzadeh, S., Matthäi, S. K., & Driesner, T. (2022b). Finite element simulations of hydraulic fracturing: A comparison of algorithms for extracting the propagation velocity of the fracture [Journal Article]. *Engineering Fracture Mechanics*, *274*, 108783. doi: 10.1016/j.engfracmech.2022.108783

Phillips, O. M. (1991). *Flow and reactions in permeable rocks* [Book]. Cambridge [etc.]: Cambridge University Press.

Ping, J., Al-Hinai, O., & Wheeler, M. F. (2017). Data assimilation method for fractured reservoirs using mimetic finite differences and ensemble kalman filter [Journal Article]. *Computational Geosciences*, *21*(4), 781-794. doi: 10.1007/s10596-017-9659-7

Pollard, D. D., & Aydin, A. (1988). Progress in understanding jointing over the past century [Journal Article]. *GSA Bulletin*, *100*(8), 1181-1204. doi: 10.1130/0016-7606(1988)100⟨1181:PIUJOT⟩2.3.CO;2

Prensky, S. E. (1999). Advances in borehole imaging technology and applications [Journal Article]. *Geological Society, London, Special Publications*, *159*(1), 1. doi: 10.1144/GSL.SP.1999.159.01.01

Pruess, K. (2002). Numerical simulation of 'multiphase tracer transport in fractured geothermal reservoirs [Journal Article]. *Geothermics*, *31*(4), 475-499. doi: 10.1016/S0375-6505(02)00007-X

Rahman, M. K., Hossain, M. M., & Rahman, S. S. (2002). A shear-dilation-based model for evaluation of hydraulically stimulated naturally fractured reservoirs [Journal Article]. *International Journal for Numerical and Analytical Methods in Geomechanics*, *26*(5), 469-497. doi: 10.1002/nag.208

Seabra, G. S., de Hoop, S., Voskov, D., & Vossepoel, F. C. (2023). Understanding of naturally fractured geothermal reservoirs using data assimilation [Conference Proceedings]. In *48th workshop on geothermal reservoir engineering*.

Shao, Q., Matthai, S., Driesner, T., & Gross, L. (2021). Predicting plume spreading during co2 geo-sequestration: benchmarking a new hybrid finite element–finite volume compositional simulator with asynchronous time marching [Journal Article]. *Computational Geosciences*, *25*(1), 299-323. doi: 10.1007/s10596-020-10006-1

Shao, Q., Matthäi, S. K., & Gross, L. (2019). Efficient modelling of solute transport in heterogeneous media with discrete event simulation [Journal Article]. *Journal of Computational Physics*, *384*, 134-150. doi: 10.1016/j.jcp.2019.01.026

Skjervheim, J.-a., Evensen, G., Hove, J., & Vabø, J. G. (2011). An ensemble smoother for assisted history matching [Conference Proceedings]. In *Spe reservoir simulation symposium* (p. 15). SPE: Society of Petroleum Engineers. doi: 10.2118/141929-MS

Smith, M. (2009). *Abaqus/standard user's manual, version 6.9* [Book]. Providence, RI: Dassault Systèmes Simulia Corp.

Thomas, R. N., Paluszny, A., & Zimmerman, R. W. (2020). Permeability of three-dimensional numerically grown geomechanical discrete fracture networks with evolving geometry and mechanical apertures [Journal Article]. *Journal of Geophysical Research: Solid Earth*, *125*(4), e2019JB018899. doi: doi.org/10.1029/2019JB018899

Torsvik, T. H., Sturt, B. A., Ramsay, D. M., Bering, D., & Fluge, P. R. (1988). Palaeomagnetism, magnetic fabrics and the structural style of the hornelen old red sandstone, western norway [Journal Article]. *Journal of the Geological Society*, *145*(3), 413-430. doi: 10.1144/gsjgs.145.3.0413

Tsang, C.-F., Neretnieks, I., & Tsang, Y. (2015). Hydrologic issues associated with nuclear waste repositories [Journal Article]. *Water Resources Research*, *51*(9), 6923-6972. doi: 10.1002/2015WR017641

Ucar, E., Berre, I., & Keilegavlen, E. (2018). Three-dimensional numerical modeling of shear stimulation of fractured reservoirs [Journal Article]. *Journal of Geophysical Research: Solid Earth*, *123*(5), 3891-3908. doi: 10.1029/2017JB015241

van Leeuwen, P. J. (2020). A consistent interpretation of the stochastic version of the ensemble kalman filter [Journal Article]. *Quarterly Journal of the Royal Meteorological Society*, *146*(731), 2815-2825. doi: 10.1002/qj.3819

van Leeuwen, P. J., & Evensen, G. (1996). Data assimilation and inverse methods in terms of a probabilistic formulation [Journal Article]. *Monthly Weather Review*, *124*(12), 2898-2913. doi: 10.1175/1520-0493(1996)124⟨2898:DAAIMI⟩2.0 .CO;2

Wang, J., Xie, H.-P., Matthai, S. K., Hu, J.-J., & Li, C.-B. (2023). The role of natural fracture activation in hydraulic fracturing for deep unconventional geo-energy reservoir stimulation [Journal Article]. *Petroleum Science*, *20*(4), 2141-2164. doi: 10.1016/j.petsci.2023.01.007

Wang, Y., Voskov, D., Khait, M., & Bruhn, D. (2020). An efficient numerical simulator for geothermal simulation: A benchmark study [Journal Article]. *Applied Energy*, *264*, 114693. doi: 10.1016/j.apenergy.2020.114693

Willis-Richards, J., Watanabe, K., & Takahashi, H. (1996). Progress toward a stochastic rock mechanics model of engineered geothermal systems [Journal Article]. *Journal of Geophysical Research: Solid Earth*, *101*(B8), 17481-17496. doi: 10.1029/96JB00882

Wu, H., Fu, P., Hawkins, A. J., Tang, H., & Morris, J. P. (2021). Predicting thermal performance of an enhanced geothermal system from tracer tests in a data assimilation framework [Journal Article]. *Water Resources Research*, *57*(12), e2021WR030987. doi: 10.1029/2021WR030987

Yao, M., Chang, H., Li, X., & Zhang, D. (2018). Tuning fractures with dynamic data [Journal Article]. *Water Resources Research*, *54*(2), 680-707. doi: 10 .1002/2017WR022019

Zhang, K., Zhang, J., Ma, X., Yao, C., Zhang, L., Yang, Y., . . . Zhao, H. (2021). History matching of naturally fractured reservoirs using a deep sparse autoencoder [Journal Article]. *SPE Journal*, *26*(04), 1700-1721. doi: 10.2118/205340-PA

Zhang, X., Huang, Z., Lei, Q., Yao, J., Gong, L., Sun, Z., . . . Li, Y. (2021).

Impact of fracture shear dilation on long-term heat extraction in enhanced geothermal systems: Insights from a fully-coupled thermo-hydro-mechanical simulation [Journal Article]. *Geothermics*, *96*, 102216. doi: 10.1016/j.geothermics.2021.102216

Zhe, L., Younis, R., & Jiang, J. (2016). A diagnostic framework for "bashed" wells in unconventional reservoirs: A numerical simulation and model selection theory approach [Conference Proceedings]. In *Spe/aapg/seg unconventional resources technology conference* (p. 17). URTEC: Unconventional Resources Technology Conference. doi: 10.15530/URTEC-2016-2448463